Comparing the permeability of shale to deionized water, liquid CO2 and NaCl solution

Shugang Yang[1] and Qingchun Yu[1]

[1]China University of Geosciences (Beijing)

November 22, 2022

Abstract

The permeability of shale is a controlling factor in fluid migration, solute transport, and overpressure development in a sedimentary basin. However, shale permeabilities measured with different fluids can be very different. To investigate the effects of fluid type on shale liquid permeability, a series of flow experiments on three samples were conducted using deionized water, liquid CO2 and 1 mol/L NaCl solution as permeating fluids. The results indicate that the liquid CO2 flow obeys Darcy's law, showing a constant permeability. The liquid CO2 permeabilities of samples C01, C02 and C03 are 6.90×10-19 m2, 3.80×10-20 m2 and 1.59×10-18 m2, respectively. The transport of the deionized water and NaCl solution in these samples deviates from Darcy's law, and threshold pressure gradient is observed. The permeabilities measured with these two fluids exhibit nearly identical ranges (10-20˜10-21 m2). The sample permeated with NaCl solution generally shows a lower permeability (under the same pressure gradient) but a higher threshold pressure gradient. The relationship between water permeability and pressure gradient follows a power function, with exponents ranging from 0.96˜3.41 for deionized water and 0.34˜3.30 for NaCl solution. The permeability reduction magnitude (ω) was defined to describe the difference between the three liquid permeabilities and the helium absolute permeability. The range of ω is 0.25˜0.96 for liquid CO2, 1.44˜2.32 for deionized water and 1.89˜3.09 for NaCl solution. The dependence of permeability on fluid type results from the differences in the fluid properties (viscosity and polarity) and fluid-mineral interactions.

Comparing the permeability of shale to deionized water, liquid CO_2 and NaCl solution

Shugang Yang, Qingchun Yu*

Beijing Key Laboratory of Water Resources and Environmental Engineering, School of Water Resources and Environment, China University of Geosciences (Beijing), 29 Xueyuan Road, Haidian District, Beijing 100083, China.

*Corresponding author: E-mail: yuqch@cugb.edu.cn

Shugang Yang: Orcid ID: 0000-0001-5452-8634

Qingchun Yu: Orcid ID: 0000-0002-7818-4829

Key points

●A permeability model taking into account the simultaneous movement of bulk water and bound water with non-Newtonian behavior is established

●Shale permeability measured with NaCl solution is the lowest due to pore compression caused by decreased electrical double layer repulsion

●Liquid CO_2 flow in shale obeys Darcy's law and the corresponding permeability is a constant, ranging from 3.80×10^{-20}~1.59×10^{-18} m^2

Abstract

The permeability of shale is a controlling factor in fluid migration, solute transport, and overpressure development in a sedimentary basin. However, shale permeabilities measured with different fluids can be very different. To investigate the effects of fluid type on shale liquid permeability, a series of flow experiments on three samples were conducted using deionized water, liquid CO_2 and 1 mol/L NaCl solution as permeating fluids. The results indicate that the liquid CO_2 flow obeys Darcy's law, showing a constant permeability. The liquid CO_2 permeabilities of samples C01, C02 and C03 are 6.90×10^{-19} m^2, 3.80×10^{-20} m^2 and 1.59×10^{-18} m^2, respectively. The transport of the deionized water and NaCl solution in these samples deviates from Darcy's law, and threshold pressure gradient is observed. The permeabilities measured with these two fluids exhibit nearly identical ranges (10^{-20}~10^{-21} m^2). The sample permeated with NaCl solution generally shows a lower permeability (under the same pressure gradient) but a higher threshold pressure gradient. The relationship between water permeability and pressure gradient follows a power function, with exponents ranging from 0.96~3.41 for deionized water and 0.34~3.30 for NaCl solution. The permeability reduction magnitude (ω) was defined to describe the difference between the three liquid permeabilities and the helium absolute permeability. The range of ω is 0.25~0.96 for liquid CO_2, 1.44~2.32 for deionized water and 1.89~3.09 for NaCl solution. The dependence of permeability on fluid type results from the differences in the fluid properties (viscosity and polarity) and fluid-mineral interactions.

Key words: shale, water permeability, liquid CO_2 permeability, fluid-rock interactions

1. Introduction

Shale and mudstone constitute approximately two-thirds of the sedimentary rock mass on Earth and play a defining role in the fluid/rock evolution of basins and in a wide range of geoengineering systems (Best & Katsube, 1995; Bourg & Ajo-Franklin, 2017; Van Noort & Yarushina, 2018). Developments in geochemical modeling and quantitative basin analysis have highlighted the key role of shales in the control of processes operating in a sedimentary basin (Best & Katsube, 1995). Shales and other argillaceous formations can function as potential host rocks for the geological disposal of nuclear waste to prevent pollutant migration and minimize the risk for biosphere contamination (Neuzil, 2013). In petroleum systems and carbon dioxide geological storage, shales are common caprocks because of their low porosity, very low permeability and high capillary entry pressure (Borysenko et al., 2009; Bourg et al., 2015). Recently, commercial extractions of shale gas/oil have helped generate a global energy boom and lower hydrocarbon costs (Middleton et al., 2015). The roles of shales played in these fields depend on the acquisition of permeability data of different fluids, which can provide a quantitative basis for elucidating not only the aforementioned processes but also basin-scale hydrogeological circulation, wellbore stability, and other topics related to subsurface hydrology.

The transient pulse decay technique and steady-state method have been employed to investigate the liquid permeability of shales or mudstones using gas, distilled water or electrolyte solution as permeates (Yang & Aplin, 2007; Armitage et al., 2011; Ghanizadeh, et al., 2014). Research indicates that the liquid permeability ranges from nanodarcy to microdarcy and is affected by various factors, including porosity, pore radius, clay fraction, effective stress, fluid properties and flow direction (Revil & Cathles, 1999; Kwon et al., 2004a, 2004b; Yang & Aplin, 2007; Bourg & Ajo-Franklin, 2017). Permeability decreases with decreasing porosity and pore radius, and increasing clay content and effective pressure (Dewhurst et al., 1999; Crawford et al., 2008; Armitage et al., 2011). Permeability measured perpendicular to bedding is commonly less than that measured parallel to bedding (Armitage et al., 2011; Ghanizadeh et al., 2014). Water permeability is lower than gas absolute permeability, which indicates that water-mineral interactions strongly affect permeability (Yang & Yu, 2020). Different salt solutions will influence the hydration states of clay and the thickness of bound water films formed on mineral surfaces,

which can influence permeability (Busch & Hildenbrand, 2013; Wilson & Wilson, 2014). A higher electrolyte concentration usually leads to a higher permeability (Mesri & Olson, 1971; Behnsen & Faulkner, 2011). However, the understanding of the variation in shale saline water permeability with pressure gradient is rarely reported. The threshold pressure gradient (TPG, below which no flow occurs) exists for deionized water flow in shale (Yang & Yu, 2020). Whether the TPG exists for 1mol/L NaCl solution flow in shale still needs to be experimentally investigated.

CO_2 geologic sequestration is considered to be an efficient solution to reduce the anthropogenic emission of CO_2 to the atmosphere and thus significantly mitigate climate change (Bourg et al., 2015; Zhang et al., 2016a; Iglauer, 2017). In the process of the extraction of oil and gas from tight formations, the economic and environmental concerns of hydraulic fracturing have resulted in the use of non-aqueous fracturing fluids, including liquid or supercritical CO_2 (Middleton et al., 2015; Al-Zaidi & Fan, 2018). The phase of CO_2 will change at different reservoir pressures and temperatures, exhibiting a gas, liquid or supercritical state (Tokunaga & Wan, 2013). Characterizing and understanding the permeability of CO_2 at different phases is crucial for both geological CO_2 storage and shale gas/oil recovery enhancement. The existing experimental studies on the CO_2 permeability of shale have been performed mainly with gaseous CO_2 or supercritical CO_2 (Van Noort & Yarushina, 2018; Zhang & Ranjith, 2018). However, there is a paucity of data on the liquid CO_2 permeability of shale. In addition, a comparative investigation of the shale permeability measured with deionized water, liquid CO_2 and NaCl solution will contribute to a further understanding of the influence of fluid-rock interfacial interactions on the magnitude of permeability.

The difficulty in measuring the permeability of tight rocks has resulted in the development of permeability models that use more easily measured parameters, such as porosity, specific surface area and tortuosity. The model currently used most often is the Kozeny-Carman equation, which was derived from pore size distribution based on the assumption that all pores are capillary tubes with identical cross sections (Yang & Aplin, 2007). Considering fluid-media interactions and the complexity of pore passages, improved Kozeny-Carman relations that consider the effective void ratio or three-dimensional rock microstructure have been proposed (Latief & Fauzi, 2012; Ren et al., 2016). Increasing interest in shale gas has resulted in the establishment of permeability models

for gas transport in shale reservoirs, which take into account gas adsorption, stress dependence, non-Darcy flow, surface diffusion and other factors (Wang et al., 2015; Song et al., 2016). By comparison, few permeability models to describe the liquid flow in shale have been proposed. According to the classical Kozeny-Carman relationship, Revil and Cathles (1999) derived a model to predict the saline water permeability of shale by using electrical parameters to distinguish pore throat porosity from the total porosity and effective hydraulic radius from the total hydraulic radius. Yang and Aplin (2010) introduced an absolute permeability formulation for mudstones that considers the influence of the void ratio and clay content but does not consider the effect of the solution chemistry. Additionally, Afsharpoor and Javadpour (2016) used computational fluid dynamics modeling with various slip and geometric conditions to investigate the effective liquid permeability of shale. On the basis of the water transport behavior in a single nanotube, Zhang et al. (2018) proposed an apparent water permeability model that fully considers the wettability, total organic carbon (TOC) content, pore size-related liquid slippage effect, and structural parameters of the shale matrix. A simplified Bingham flow model has also been proposed to illustrate that the water permeability of sandstone increases with increasing pressure gradient (Tanikawa & Shimamoto, 2009). However, water in saturated shale is composed of bound water and free water (Yang & Yu, 2020), and permeability models that take the simultaneous movement of free water and bound water into consideration have rarely been reported.

This study is aimed at investigating different liquid permeabilities of shale samples collected from the Qaidam Basin, China. Permeability measurements were performed on three samples at various pressure differences and a constant confining pressure using helium, deionized water, liquid carbon dioxide and sodium chloride solution as pore fluids. By using different fluids to measure the permeability of the same sample, it was intended to obtain insights into the influence of fluid-rock interactions on the permeability of shales. The flow rates and permeabilities of different fluids were measured at different pressure gradients. The relationships between the flow rate and pressure gradient and between the permeability and pressure gradient were established. Based on the distributions of water with different movabilities in the shale nanopores, a permeability model considering the simultaneous movement of bulk water and bound water with non-Newtonian behavior is established. The permeability reduction magnitude was newly defined

to quantitatively compare the permeabilities of the three liquids using helium absolute permeability as a reference value. The effects of mineral composition and pore structure on the permeability reduction magnitude were discussed.

2. Methodology

2.1. Materials

2.1.1. Experimental samples

The shale samples used in the experiments were collected from the Carboniferous formation in the eastern Qaidam Basin, China, at depths between 106 m and 404 m. Three cylindrical samples were drilled from the shale cores perpendicular to the bedding plane and were labeled samples C01, C02 and C03. Both sides of the specimens were ground smooth. The initial dimensions of the sample plugs were 25 mm in diameter and 13~24 mm in length. The mineral compositions of shale samples were determined by X-ray diffraction analysis and the TOC content was measured by a LECO carbon sulfur analyzer. The results indicate that quartz, calcite and clay are the dominant minerals, with traces of dolomite, feldspar and pyrite. The total clay proportion was approximately 30%, and the clay mineralogy of the samples is dominated by illite clay, as discrete illite and mixed-layer illite/smectite. The TOC values fall in the range of 0.55%~0.95%. A detailed description of the mineral composition and organic matter properties of these samples can be found in our previous study (Yang & Yu, 2020).

Shales generally have much smaller (orders of magnitude) permeabilities than sandstones and carbonate rocks due to their nanoscale pore structures. The pores in shale can be categorized into micropores (d<2 nm), mesopores (d=2~50 nm), and macropores (d>50 nm) by diameter (Loucks et al., 2012). To comprehensively describe the pore structure parameters and pore size distributions of the samples, mercury intrusion porosimetry, low-pressure N_2 adsorption and low-pressure CO_2 adsorption experiments were performed. A detailed description of the measurement methodology is presented by Wang and Yu (2016). The pore size distributions of samples C01, C02 and C03 are presented in Figure 1, which indicates that the samples display extremely small pores, mainly concentrated in the 0.4~50 nm range. The proportions of pores with diameters smaller than 50 nm account for 69%~88% of the total pore volume. The peak value in

Figure 1 indicates that the most probable pore diameter in the three samples is approximately 20 nm. These distribution modes represent the pore sizes of the main fluid flow paths in the samples, thus providing a qualitative explanation for their low permeabilities.

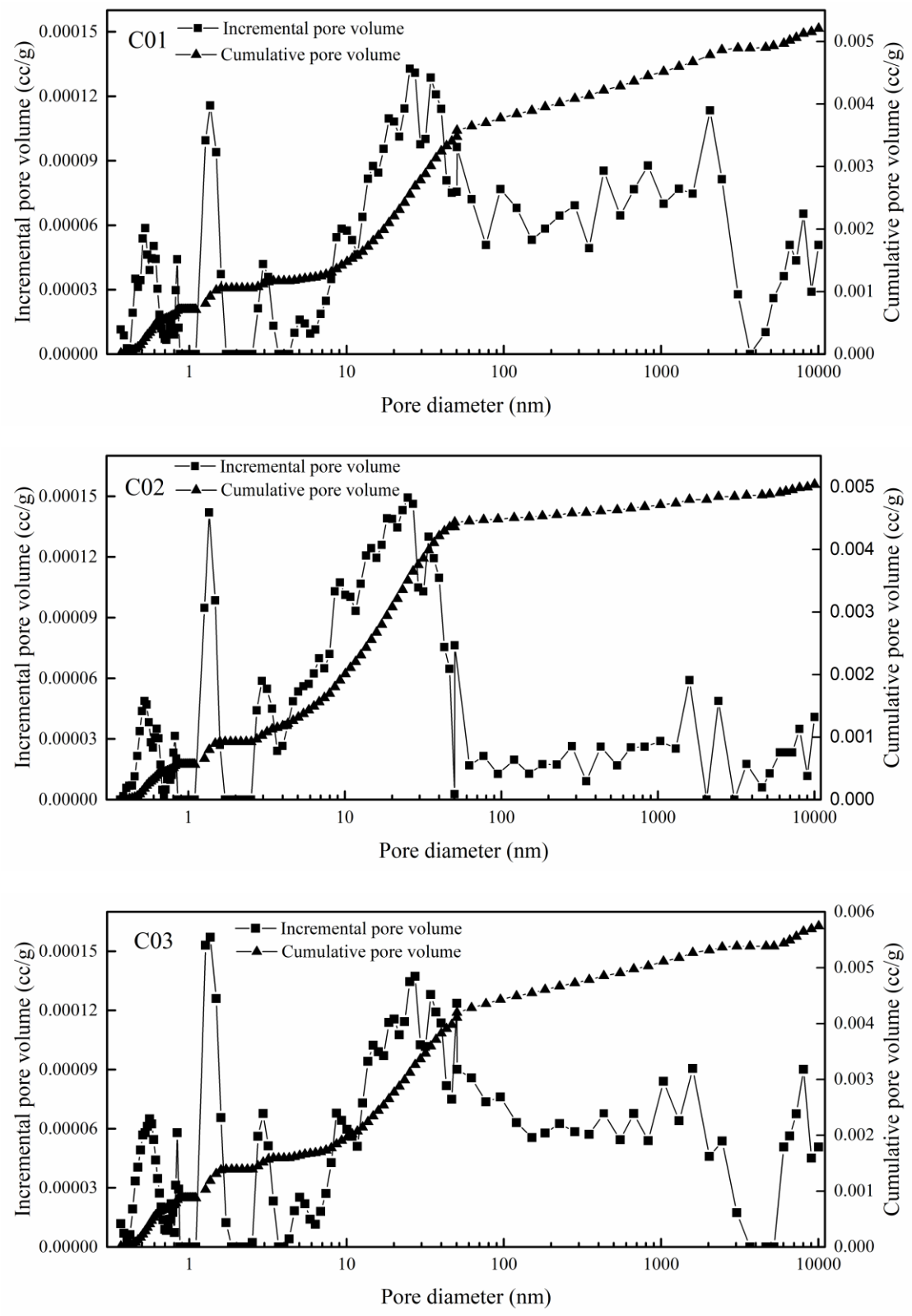

Figure 1. Pore size distributions of the shale samples (low-pressure CO_2 adsorption for diameters less than 2 nm,

low-pressure N_2 adsorption for diameters ranging from 2 to 50 nm, and high-pressure mercury intrusion for diameters larger than 50 nm).

The total porosity and cumulative specific surface area of the samples can also be determined by gas adsorption and mercury intrusion experiments (Wang & Yu, 2016; Zhang & Yu, 2019). As shown in Table 1, the porosity values of samples C01, C02 and C03 are 1.36%, 1.30% and 1.52%, respectively. The specific surface area values of the samples range from 6.85~9.83 m^2/g, suggesting that strong interfacial interactions will occur as polar fluid is introduced. In addition, the interpretation of mercury intrusion porosimetry data could be used to acquire the tortuosity, bulk density, pore/throat ratio and compressibility of the sample (Carlos, 1998), which are presented in Table 1. Note that the measured pore/throat ratio is related to the percent porosity filled. The values listed in Table 1 correspond to the respective maximum percent porosities filled. For samples C01, C02 and C03, the maximum percent porosities filled are 100%, 91% and 96%, respectively.

Table 1 The lengths, pore structure parameters and compressibility of the shale samples.

Sample number	Length (cm)	Total porosity (%)	Cumulative specific surface area (m^2/g)	Tortuosity	Pore percentage (%)	Pore-throat ratio	Compressibility factor (1/psi)
C01	2.42	1.36	7.85	2.33	68.72	57.56	2.49×10^{-7}
C02	2.40	1.30	6.85	2.22	87.99	12.94	5.73×10^{-8}
C03	1.31	1.52	9.83	2.39	73.04	17.76	3.50×10^{-7}

Note. The pore percentage refers to the ratio of the micro-meso-pore volume to the total pore volume.

2.1.2. Experimental fluids

The fluids used to investigate liquid permeability in this study include helium, deionized water, liquid CO_2 and 1 mol/L NaCl solution.

High-purity helium is used as the permeating fluid to obtain the absolute permeability (Klinkenberg-corrected permeability) of the shale samples. The helium molecule is small and is able to flow through extremely small pore throats that are not accessible to the other gases (Sander et al., 2017). In addition, helium is a noble gas with extremely low absorptivity to shales and thus will not affect the shale matrix (Fakher & Imqam, 2020), which means that the fluid-rock

interfacial interactions are negligible.

Deionized water was chosen because its polar interactions are much more complex than those of simple nonpolar liquids. These interactions involve hydrogen bonds, hydration forces and electrostatic interactions. As a consequence, water has a high affinity for hydrophilic mineral surfaces and a tendency to completely spread over them. This results in the formation of bound water, which exhibits considerably different properties and structures compared with bulk water and can negatively affect the movement of water.

Unlike water, CO_2 has a zero external electrical dipole moment and a low dielectric constant (Iglauer, 2017). In addition, liquid CO_2 is a weakly polar fluid (Lundin et al., 2015). Using liquid CO_2 as the testing fluid can theoretically reduce the effect of the fluid-rock interactions on the transport of fluid and can also be used to analyze the influence of fluid polarity on permeability.

The diffuse layer in the electrical double layer (EDL) formed on mineral surfaces controls various transport properties, including the electrical conductivity, osmotic efficiency coefficient, and streaming potential coupling coefficient (Revil et al., 2011). At the high salinity limit (typically >0.5 mol/L), the diffuse layer disappears, and the counterions are packed in the Stern layer; outside the Stern layer, the pore water has the same salinity as the pore water (Revil & Leroy, 2004). To remove the influence of the diffuse layer and maximize the contrast between the test results of the deionized water and the solution, the 1 mol/L NaCl solution was used as the permeating fluid (solubility of NaCl, 35.9 g/100 g at room temperature), which was obtained by dissolving weighed quantities of reagent-grade salts in deionized water. The NaCl solution was chosen because sodium is usually part of the chemical composition of hydraulic fracturing fluids and is also present in shale pore water (Roshan et al., 2015).

2.2. Permeability experiments

Both the steady-state technique and unsteady-state method (e.g., the pressure pulse decay method) have been used in shale permeability tests (Sander et al., 2017). Given that the unsteady-state method may overestimate permeability and has difficulty obtaining flow rate data, the steady-state method is used for all the experiments, although it is time-consuming. The permeability experiments conducted in this study can be categorized into three sets. In set 1,

experiments of single-phase helium and water flow were conducted. The objective of this set was to obtain the absolute permeability and water permeability of the samples. This work was completed in our previous study (Yang & Yu, 2020). In set 2, the liquid CO_2 permeability of the samples was measured. In set 3, NaCl solution permeability experiments were conducted. The purpose of sets 2 and 3 was to investigate the effects of fluid-shale interfacial interactions on permeability.

2.2.1. Experimental apparatus

The experimental apparatus used to measure permeability is shown in Figure 2. It mainly consists of the following parts: (1) a core holder with a rubber sleeve, which was set horizontally in the thermostat. (2) A fluid injection system controlled by a high-pressure constant-flow pump or pressure-reduction valve. With this apparatus, fluid can be injected at a constant pressure, with an accuracy of 0.01 MPa, into the core holder. (3) A confining and back pressure system, which was used to create and maintain the confining pressure (around the rock sample) and back pressure (at the outlet of the core holder). The injection pressure was at least 5 MPa lower than the confining pressure to reduce the possibility of hydraulic fracturing within the shales and fluid leakage from the gap between the rubber sleeve and the sample (Zhang & Yu, 2019). The fluid flowed out only when the pressure exceeded the back pressure. (4) A vacuum pump, which was used to remove the air from the core holder and the pipelines. (5) A data acquisition system, which was used to record the pressures upstream and downstream of the core holder and the temperature once per minute. (6) A thermostat system, which was used for adjusting and maintaining the experimental temperature.

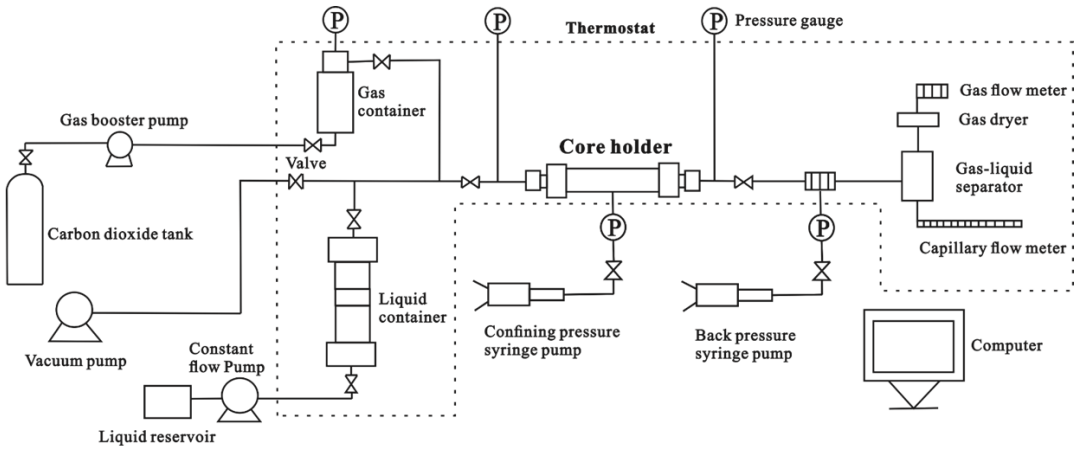

Figure 2. Schematic diagram of the apparatus used for the liquid permeability experiments, improved from Yang and Yu (2020).

2.2.2. Permeability tests

The water permeability experiments were carried out at a constant temperature of 30 ℃ and a constant confining pressure of 15 MPa. Permeability was measured at 6~8 constant water pressure differences that stepped down from the maximum value (9.5 MPa for C01 and C02, 7.4 MPa for C03) to the minimum value (approximately 2 MPa). The maximum pressure was maintained for approximately 4~8 days to remove the residual gas from the system. Individual permeability tests took approximately 2~3 days to perform, depending upon the permeability of the sample and the pressure conditions. The water flow volume was measured as a function of time by a capillary flow meter. When the measured water flow rate was less than 1×10^{-7} mL/s, the water pump and the valve at the entrance of the core holder were shut; the water was let through the sample at the residual pressure to obtain the TPG. A detailed description of the experimental processes can be found in Yang and Yu (2020).

When a water permeability experiment was finished, the sample was carefully removed from the apparatus and dried again. After that, the liquid CO_2 permeability was measured under the same confining pressure. Before the liquid CO_2 experiment, sample C03 had to be ground smooth again because of edge damage, causing its actual length to be 8 mm in subsequent tests. The physical properties of CO_2 (e.g., density and viscosity) are highly pressure/temperature-dependent. As shown in Figure 3, there exists a sudden change in viscosity and density when the pressure is greater than the critical point, which means that gaseous CO_2 changes into liquid CO_2. Changes in state have a great effect on fluid viscosity, density, and consequently shale permeability. To more easily reach the liquid state of CO_2 and avoid the supercritical state (which is reached at 31.8 ℃ and 7.38 MPa), the experiments were conducted at room temperature (19~22 ℃). The back pressure was applied and increased to a value greater than the critical pressure of the gaseous CO_2 for liquid permeability measurement. A set of liquid permeability measurements was conducted by increasing the back pressure from 6.4 to 7.0 MPa and adjusting the inlet pressure to create different pressure differences. The liquid CO_2 flow rate was measured under ambient conditions using a gas flow meter and converted to the flow rate at the corresponding mean pressure

according to mass conservation.

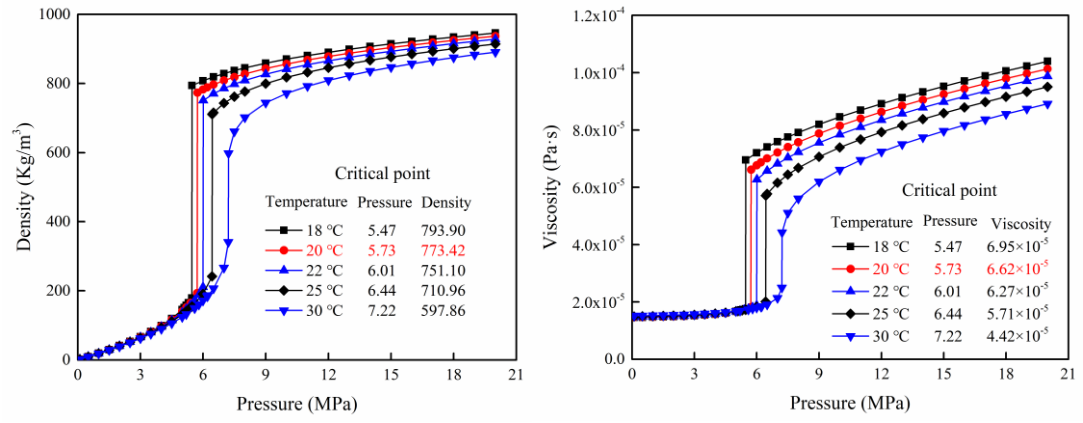

Figure 3. The density and viscosity of carbon dioxide at different pressures and temperatures. The values under different conditions were calculated using REFPROP software, which was developed by the National Institute of Standards and Technology (Zhang & Yu, 2019).

With the completion of the liquid CO_2 permeability experiments, the back pressure and inlet pressure were slowly decreased to the atmospheric pressure. The samples were carefully removed from the core holder and prepared for NaCl solution permeability experiments. The experimental process and conditions used to measure the saline water permeability were consistent with those used to measure the deionized water permeability. The only difference was that the vacuuming time was extended before the pre-saturation experiments to reduce the effect of the dissolution of residual CO_2 on the pore structure. During the saturation experiments, the edge of sample C01 was damaged. The sample was ground smooth again, resulting in an actual length of 12.42 mm for the NaCl solution permeability experiments.

When the fluid flow reached steady state at a certain pressure difference, the permeabilities of the deionized water, liquid CO_2 and NaCl solution were calculated according to Darcy's law (Hildenbrand et al., 2004; Dong et al., 2012; Ghanizadeh et al., 2014; Zhang et al., 2016a):

$$k_{w,lc,NaCl} = \frac{Q_{w,lc,NaCl} \cdot \mu L}{A(p_1 - p_2)} \#(1)$$

where $k_{w,lc,NaCl}$ refers to the permeability of the deionized water, liquid CO_2, and NaCl solution, $Q_{w,lc,Na}$ is the flow rate of the corresponding fluid, L is the sample length, A is the cross-sectional area of the sample, and p_1 and p_2 are the upstream and downstream pressures, respectively. The parameter μ is the viscosity of the fluid. For the deionized water, the effective viscosity is used for

calculation (Yang & Yu, 2020); for the liquid CO_2, the viscosity is shown in Figure 3; for the 1 mol/L NaCl solution, the viscosity at 30 ℃ is approximately 0.872 mPa·s based on the viscosity value at 20 ℃ (1.1 mPa·s) and the relationship between the viscosity and temperature of water (Kwon et al., 2004b; Chapuis, 2012).

3. Results and discussion

3.1. Shale permeability

The experimental results of water flow are presented in detail in Yang and Yu (2020). To intuitively compare these results with the results of the other two fluids, the measured water flow rates and their corresponding permeabilities under different pressure gradients are cited here and shown in Figure 4. It can be seen that no flow occurred when the pressure gradient was less than the TPG. The water flow in the shale pores deviates from Darcy's law and shows characteristics of plastic flow. The calculated water permeabilities of the three samples were no longer constant because of the nonlinear relationship between the flow rate and pressure gradient. The measured water permeabilities ranged from 10^{-20}~10^{-21} m^2 and increased rapidly with increasing pressure gradient. A similar phenomenon was also found in sandstones, in which the water permeability increased slightly with increasing pressure gradient (Tanikawa & Shimamoto, 2009).

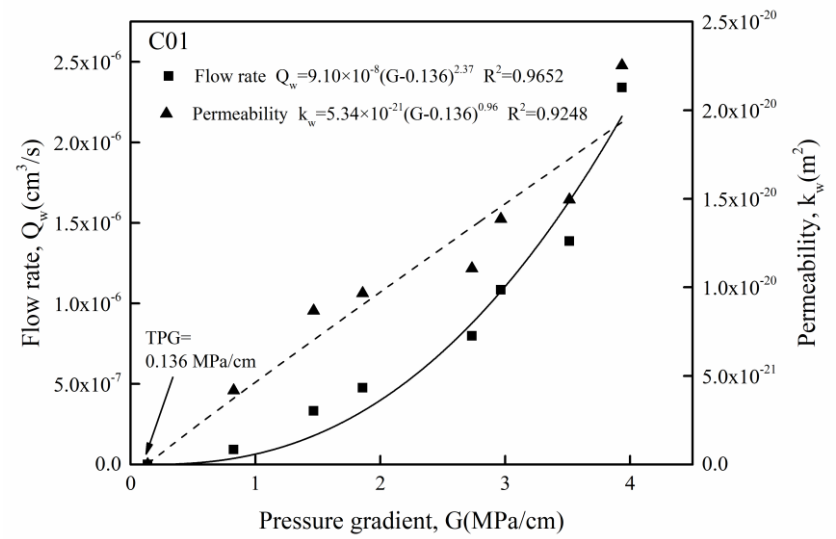

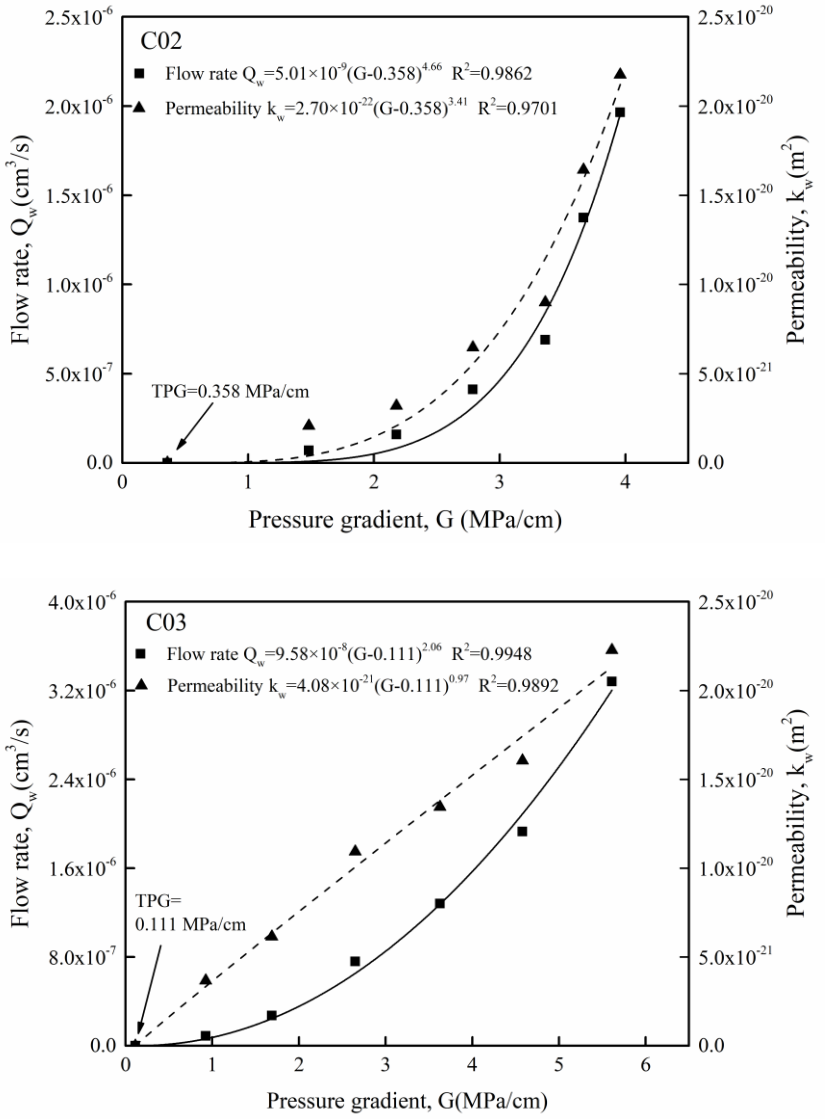

Figure 4. The measured water flow rates and the corresponding permeabilities under different pressure gradients. This dataset was obtained in our previous work (Yang & Yu, 2020).

When liquid CO_2 was used as the permeating fluid, the flow experiments conducted on the same sample indicated no measurable deviation from Darcy's law under the experimental conditions. The flow rate vs. pressure gradient curve is a straight line that passes through the origin (Figure 5). No TPG was observed. The liquid CO_2 permeability remained approximately constant with increasing pressure gradient. For samples C01, C02 and C03, the permeabilities are 6.90×10^{-19} m^2, 3.80×10^{-20} m^2 and 1.59×10^{-18} m^2, respectively. Similar experimental results have also been reported for siltstones, in which the movement of liquid CO_2 obeys Darcy's law; the measured permeabilities were reported to be constants with values of 3.5×10^{-18} m^2 and 3.2×10^{-18}

m^2 (Dong et al., 2012).

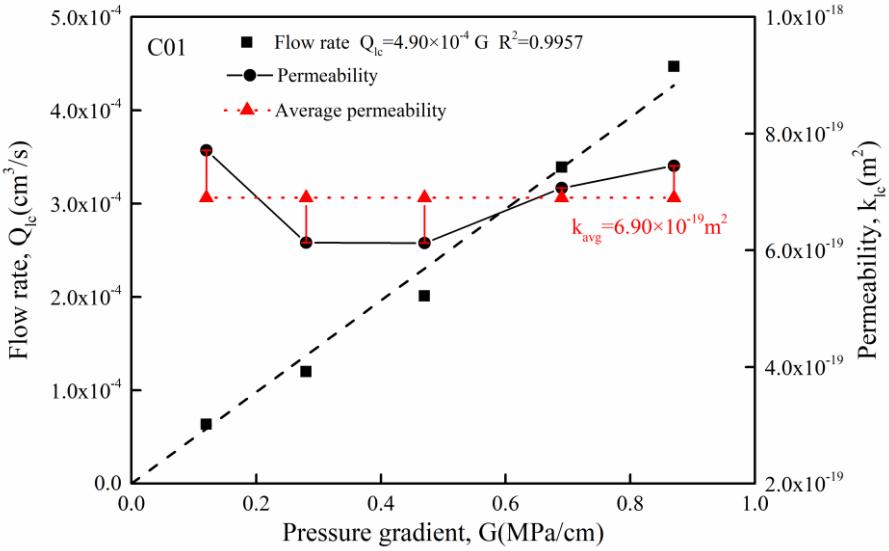

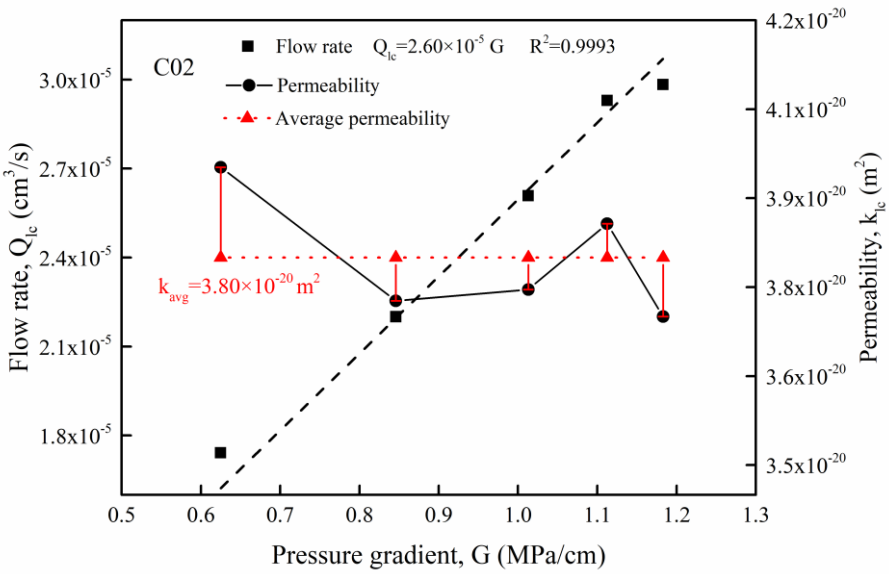

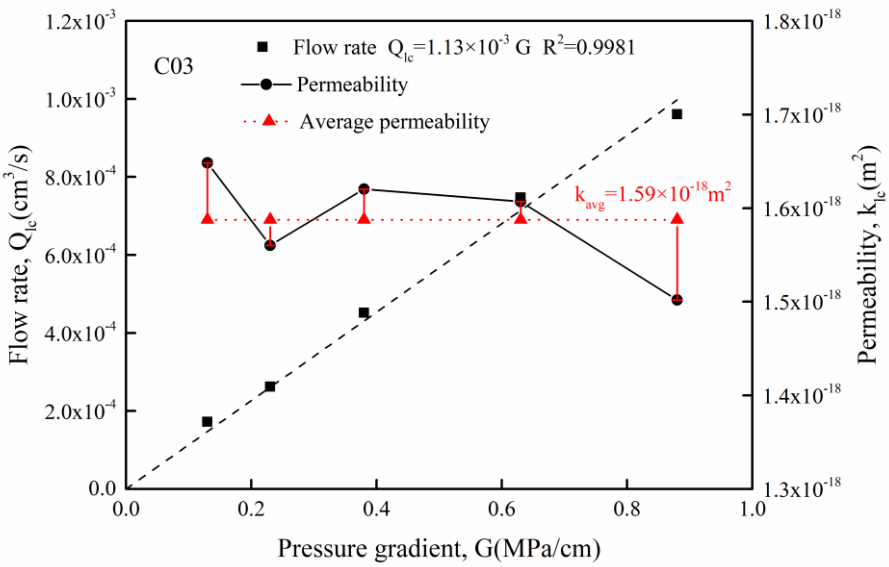

Figure 5. Measured liquid CO_2 flow rates and the corresponding permeabilities under different pressure gradients.

The experimental process of the NaCl solution flow experiments is shown in Figure 6, in which the pressure differences are plotted as a function of time. Similar to the procedure for the deionized water, each measurement was divided into high pressure displacement, step-by-step depressurization and natural depressurization processes. Considering that the final steady pressure differences of the three repeated tests were approximately equal when the deionized water was used as the permeate (Yang & Yu, 2020), the natural depressurization process for the NaCl solution flow tests was only carried out once. Although the calculation results show that the diffuse layer thickness was as low as 0.3 nm and thus could be neglected (Revil & Leroy, 2004; Tokunaga, 2011) when the concentration of NaCl solution was as high as 1 mol/L, the final steady (or pseudo-steady) pressure differences for the three samples were still greater than zero. This indicates that the movement of the 1 mol/L NaCl solution in the shale nanopores still need to reach a critical pressure to overcome the flow resistance under the experimental conditions. The results of the NaCl solution flow experiments are presented in Figure 7. The measured flow rates were 10^{-6}~10^{-7} mL/s, and the movement of the NaCl solution did not obey Darcy's law, showing the characteristics of deionized water flow. The permeabilities were in the range of 10^{-20}~10^{-21} m^2 and increased with increasing pressure gradient in the form of a power function.

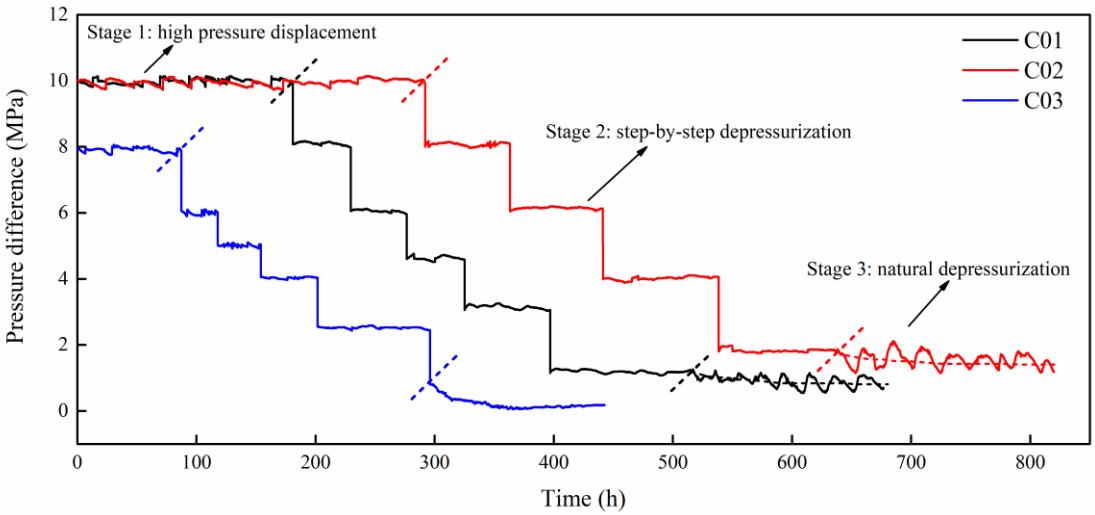

Figure 6. The variation in the pressure difference between the two ends of the sample (1 mol/L NaCl solution).The final pseudo-steady pressures for samples C01 and C02 at the natural depressurization stage fluctuate due to the fluctuation in room temperature. The average value at the trough of pressure difference curve is taken as the

threshold pressure.

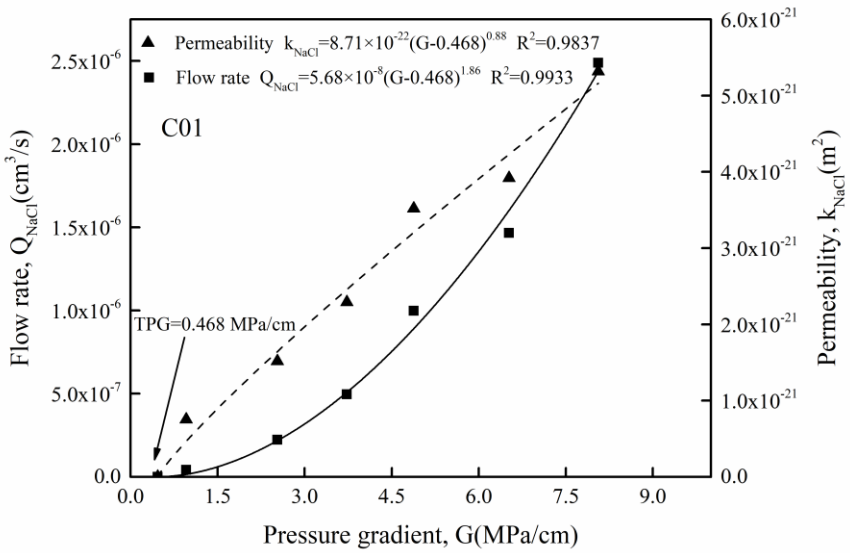

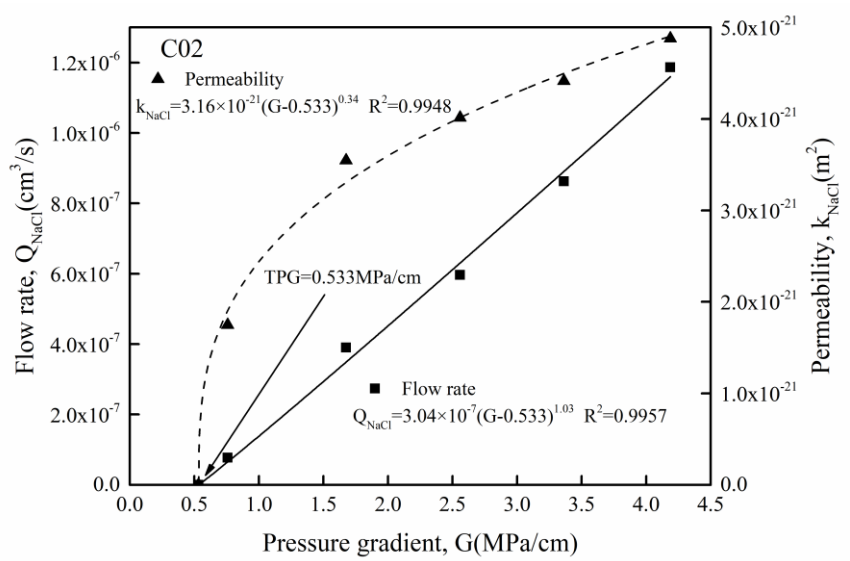

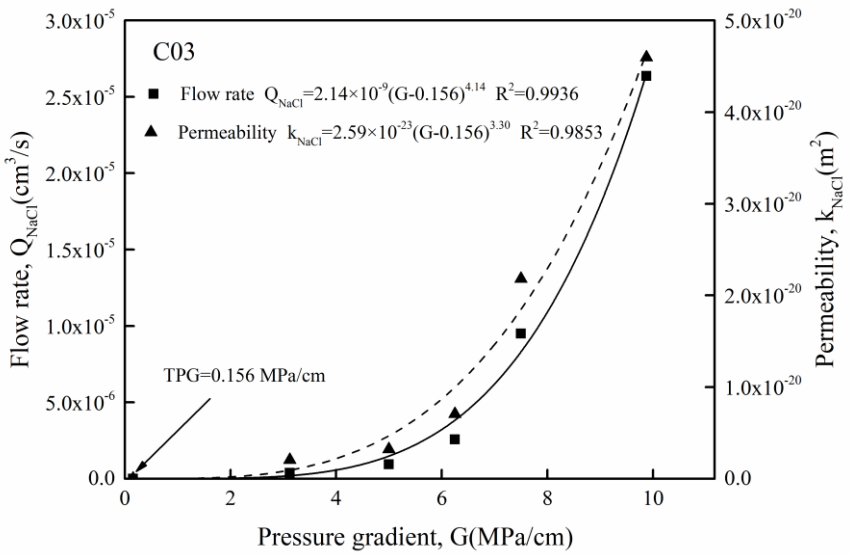

Figure 7. Measured NaCl solution flow rates and the corresponding permeabilities under different pressure gradients.

The fitting curves plotted in Figures 4-6 show that the regression equations, both for the flow rate and permeability, can be expressed by power functions:

$$Q_{w,lc,NaCl} = \gamma_1 (G - G_T)^{\beta_1} \; G \geq G_T \#(2a)$$

$$k_{w,lc,NaCl} = \gamma_2 (G - G_T)^{\beta_2} \; G \geq G_T \#(2b)$$

where γ and β are the fitting parameters, $G = (p_1 - p_2)/L$ is the pressure gradient, and G_T is the TPG. The fitting results and fitting parameters are listed in Table 2. The liquid permeability can be obtained by taking the derivative of the expression of the flow rate, and hence, it can be found in Table 2 that the exponent β_1 is approximately 1 larger than the exponent β_2. If the fluid flow obeys Darcy's law (for example, liquid CO_2), Eq. (2b) reduces to a constant because the G_T and β_2 are zero in that case. For deionized water, the exponent β_1 and β_2 of sample C02 are larger than that of the other two samples. While for NaCl solution, the exponents (both for β_1 and β_2) of sample C03 are obviously larger than the other two samples. In addition, the TPGs obtained from the NaCl solution flow experiments are higher than those obtained from the deionized water flow tests.

Table 2 The fitting equations and parameters of flow rate and permeability for the deionized water, liquid CO_2 and 1 mol/L NaCl solution.

Sample number	Fitting equations		G_T (MPa/cm)	β_1	β_2
	Flow rate	Permeability			
C01	$Q_w = 9.10\times10^{-8}(G\text{-}0.136)^{2.37}$	$k_w = 5.34\times10^{-21}(G\text{-}0.136)^{0.96}$	0.136	2.37	0.96
	$Q_{lc} = 4.90\times10^{-4}G$	$k_{lc} \approx 6.90\times10^{-19}$	0	1	0
	$Q_{NaCl} = 5.68\times10^{-8}(G\text{-}0.468)^{1.86}$	$k_w = 8.71\times10^{-22}(G\text{-}0.468)^{0.88}$	0.468	1.86	0.88
C02	$Q_w = 5.01\times10^{-9}(G\text{-}0.358)^{4.66}$	$k_w = 2.70\times10^{-22}(G\text{-}0.358)^{3.41}$	0.358	4.66	3.41
	$Q_{lc} = 2.60\times10^{-5}G$	$k_{lc} \approx 3.80\times10^{-20}$	0	1	0
	$Q_{NaCl} = 3.04\times10^{-7}(G\text{-}0.533)^{1.03}$	$k_w = 3.16\times10^{-21}(G\text{-}0.533)^{0.34}$	0.533	1.03	0.34
C03	$Q_w = 9.58\times10^{-8}(G\text{-}0.111)^{2.06}$	$k_w = 4.08\times10^{-21}(G\text{-}0.111)^{0.97}$	0.111	2.06	0.97
	$Q_{lc} = 1.13\times10^{-3}G$	$k_{lc} \approx 1.59\times10^{-18}$	0	1	0
	$Q_{NaCl} = 2.14\times10^{-9}(G\text{-}0.156)^{4.14}$	$k_w = 2.59\times10^{-23}(G\text{-}0.156)^{3.30}$	0.156	4.14	3.30

The permeabilities of the samples measured with the three liquids are summarized in Table 3. For the same sample, the liquid CO_2 permeability remains constant and is higher than that of water, suggesting that fluid polarity and fluid-rock interactions play an important role in the magnitude of permeability. The measured NaCl solution permeability is less than the water permeability. When the pressure gradient is approximately 3.5 MPa/cm, the deionized water permeability is approximately 3~7 times larger than the NaCl solution permeability. Added salt confines the bound water to the first monolayer, and hence, reduces the thickness of the bound water (Holt & Kolsto, 2017). Theoretically, the NaCl solution permeability should be larger than the deionized water permeability when the ionic concentration is as high as 1 mol/L. This contradiction would be discussed in Section 3.2.3.

Table 3 The permeabilities of shale samples measured with different fluids.

Sample number	Permeability (m^2)					
	Helium	Deionized water		Liquid CO_2	1mol/L NaCl solution	
		Range	G≈3.5 MPa/cm		Range	G≈3.5 MPa/cm
C01	2.52×10^{-18}	4.18×10^{-21}-2.25×10^{-20}	1.50×10^{-20}	6.90×10^{-19}	7.54×10^{-22}-5.32×10^{-21}	2.22×10^{-21}
C02	3.48×10^{-19}	2.07×10^{-21}-2.18×10^{-20}	1.27×10^{-20}	3.80×10^{-20}	1.86×10^{-21}-4.88×10^{-21}	4.49×10^{-21}
C03	2.82×10^{-18}	3.66×10^{-21}-2.23×10^{-20}	1.35×10^{-20}	1.59×10^{-18}	2.05×10^{-21}-4.60×10^{-20}	2.29×10^{-21}

Note. The shale absolute permeability measured with helium is referred to Yang and Yu (2020)

3.2. Discussion

3.2.1. The dependence of permeability on pressure gradient

The aforementioned experimental results indicate that shale permeabilities measured with the deionized water and NaCl solution are related to the pressure gradient and TPG, while the permeability measured with the liquid CO_2 is approximately a constant and is independent of the pressure gradient. This phenomenon can be explained by the following permeability model.

The pore geometry in shale is significantly complex and highly variable, including cylindrical, angular, and slit-shaped pores (Loucks et al., 2012; Afsharpoor & Javadpour, 2016). This work adopts the cylindrical pore assumption to establish the liquid permeability model. Given that the liquids used in this study are deionized water, sodium chloride solution and liquid CO_2, the permeability model is first deduced taking deionized water as an example. The

permeability models of the other two liquids can be derived on the basis of the simplification of the former model.

Owing to the strong water-rock interactions in shale, the structural and dynamic properties (e.g., viscosity) of bound water formed on shale mineral surfaces dramatically deviate from those of bulk water. Under a specific pressure gradient, the water flow in shale nanopores is actually the simultaneous movement of free water and bound water. Thus, the conventional permeability model is not applicable. In this work, a permeability model that considers the simultaneous movement of free water and bound water with non-Newtonian behavior is derived. The details of this derivation process is presented in Appendix A. It is assumed that the pore structure remains unchanged under the experimental pressure due to the existence of EDL repulsion. The permeability model is as follows:

$$k = \frac{\phi_e}{8\tau}\left[\frac{\mu_e}{\mu_w}\frac{r_{tp}^4}{r_e^2} + \frac{\mu_e}{\mu_i}\left(r_e^2 - \frac{r_{tp}^4}{r_e^2}\right) + \frac{4}{3}\frac{\mu_e}{\mu_i}\frac{2Lf_0\left(r_{tp}^3 - r_e^3\right)}{\Delta P r_e^2}\right] \#(3)$$

where k is the permeability, ϕ_e is the effective porosity, τ is the tortuosity; μ_w, μ_i, and μ_e are the bulk water viscosity, bound water viscosity, and effective viscosity, respectively; r_e is the flow radius; r_{tp} is the distance from the pore centerline to the threshold plane (Figure A1); f_0 is the critical yield strength; ΔP is the pressure difference and L is the length. Eq. (3) denotes that for porous media with nanopores and strong water-rock interactions, the water permeability is closely related to the TPG and pressure gradient. The changes in water viscosity should also be taken into account when calculating the water permeability.

For the movement of Newtonian fluid without fluid-rock interfacial interactions and medium deformation, Eq. (3) reduces to:

$$k = \frac{\phi R^2}{8\tau} \#(4)$$

where ϕ is the porosity. The helium absolute permeability can be approximated with Eq. (4).

3.2.2. Deionized water vs. liquid CO_2

Pore throats available for fluid flow are easily modified by the formation of an adsorption layer at the mineral surfaces. Mesri and Olson (1971) reported that the permeabilities of pure clays measured with nonpolar liquids (benzene and carbon tetrachloride) are higher than those measured with polar liquids (water of varying ionic concentration), which proves that interfacial interaction

is an important factor influencing of permeability. The experimental results of this work indicate that the liquid CO_2 permeability of shale is the highest permeability measured, followed by that of the deionized water, and that the 1 mol/L NaCl solution permeability is the lowest permeability measured. To quantitatively compare the permeabilities of the three liquids, the parameter (ω) was defined to represent the permeability reduction magnitudes of the three liquids using helium absolute permeability as a reference value. The expression of ω is as follows:

$$\omega = \log_{10} \frac{k_{He}}{k_{w,lc,NaCl}} \#(5)$$

Given that the permeabilities measured with the deionized water and NaCl solution depend on the pressure gradient, the values at a pressure gradient of 3.5 MPa/cm were used for this analysis. The calculated permeability reduction magnitudes for the different fluids and samples are shown in Figure 8.

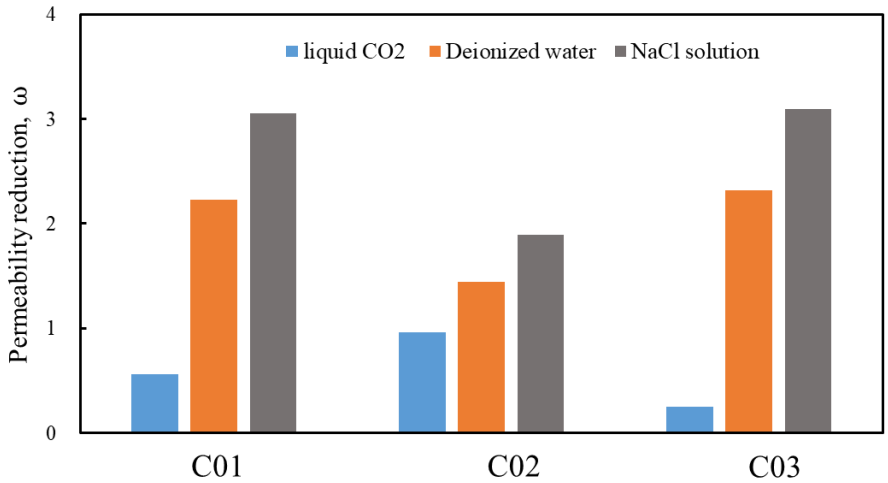

Figure 8. Difference between the helium and liquid permeabilities of shale samples.

Figure 8 shows that the liquid CO_2 permeability of a shale sample is several times lower than the helium absolute permeability but is dozens of times higher than the deionized water permeability. Liquid CO_2 is a weakly polar fluid with a high adsorption capacity, low viscosity, high density and easy seepage diffusion, which makes it advantageous to be used in enhanced coalbed methane (ECBM) extraction and organic synthesis (Lundin et al., 2015; Wei et al., 2021). The experimental results of CO_2 adsorption in shale have shown that liquid CO_2 has a higher adsorption capacity than gas and supercritical CO_2 (Fakher & Imqam, 2020). For liquid CO_2, Eq. (3) becomes:

$$k = \frac{\phi_e r_e^2}{8\tau} \#(6)$$

Compared with the helium absolute permeability, the adsorption of CO_2 on shale mineral surfaces could immobilize CO_2 and block part of the flow channel network, resulting in a decrease in the effective porosity and flow radius and thus reducing the sample permeability (Song & Zhang, 2013; Sander et al., 2017). The magnitude of the decrease in permeability is closely related to the mineral composition and pore structure of a sample.

Compared with the deionized water, liquid CO_2 not only showed higher permeability but also presents different flow rate/permeability-pressure gradient relationships (Table 2 and Table 3). This is attributed to the difference in the fluid properties and the strength of fluid-rock interfacial interactions. Water is a polar fluid with an electrical dipole moment of 6.186×10^{-30} C·m and a relative dielectric constant of 78.54, while the electrical dipole moment and static dielectric constant (at 6 MPa and 293 K) of CO_2 are 0 and 1.48, respectively (Tokunaga, 2009; Iglauer, 2017). Water molecules are more susceptible to interacting with the shale surface because of the polarized nature of the water molecule and the existence of free charge on the mineral surface, causing the formation of bound water with properties different from those of the bulk phase. According to our previous work (Yang & Yu, 2020), the movability of bound water is related to the distance from the solid surface. From the solid surface to the pore central line, water exhibits immobility, shear fluidity, electro-viscosity effect and free flow. When hydrostatic pressure is applied, the increase in movable water content with the pressure gradient leads to an increase in water permeability. By comparison, the interactions between liquid CO_2 and the solid surface are much smaller due to the weak polarity of liquid CO_2. Apart from the adsorption layer close to the mineral surfaces, most of the liquid CO_2 in shale pores is weakly affected by the solid surface and still exhibits the properties of a bulk fluid, thus resulting in a high and basically constant permeability.

3.2.3. Deionized water vs. NaCl solution

The results presented in Table 2, Table 3 and Figure 8 indicate the following trends: (1) the permeabilities measured with the NaCl solution and deionized water exhibit nearly identical ranges (10^{-20}~10^{-21} m^2). Similar experimental results have also been reported by Kwon et al.

(2004b), where the Wilcox shale permeabilities measured with distilled water, 1 mol/L NaCl solution and 1 mol/L KCl solution differ by only ~20%. (2) The shale samples show a lower permeability (G≈3.5 MPa/cm) but a larger TPG when permeated with NaCl solution. (3) Both the deionized water and NaCl solution permeabilities increase with increasing pressure gradient following a power function. Sample C02 has the largest power function exponent when permeated with the deionized water, while sample C03 has the largest power function exponent when permeated with the NaCl solution.

In general, increasing the salt concentration caused the permeability of tight media to increase relative to that obtained with deionized water. Experimental results from flow experiments performed on sandstones and clay-sand mixtures have shown that permeabilities to deionized water are significantly lower than permeabilities to ionic solutions and that the permeabilities measured with higher ionic concentrations are higher (Wei et al., 1986; Studds et al., 1998; Zhang & Sheng, 2017). In addition to ionic concentration, ionic valence also affects the magnitude of permeability. The permeability is generally lower when the adsorbed cations are monovalent rather than divalent (Mesri & Olsen, 1971; Kwon et al., 2004b).

Different mechanisms have been proposed in the literature to explain the influence of ionic concentration on permeability, including compressed EDL, reduced wettability and electric-viscous effects. The ionic concentration has a significant impact on wettability, and a higher ionic concentration results in a higher contact angle (Roshan et al., 2015, 2016; Iglauer, 2017; Pan et al., 2019). The wettability test results obtained in this work also show that the contact angle measured with the 1 mol/L NaCl solution is twice that measured with the deionized water (Figure 9). Dissolved ions (of opposite charge) move toward the charged surface, resulting in a rapid decay in the electrical potential, which reduces the surface polarity but increases the zeta potential. This reduced surface polarity and increased zeta potential results in a lower hydrophilicity; thus, the contact angle increases (Iglauer, 2017; Pan et al., 2019). In addition, the dielectric constant of the 1 mol/L NaCl solution is 63 (77.6 for water at T = 300 K), and a lower dielectric constant consequently increases the contact angle (Levy et al., 2012; Roshan et al., 2016). An increased contact angle results in a decrease in the wettability of the shale mineral surface, thus reducing the strength of the water-rock interactions.

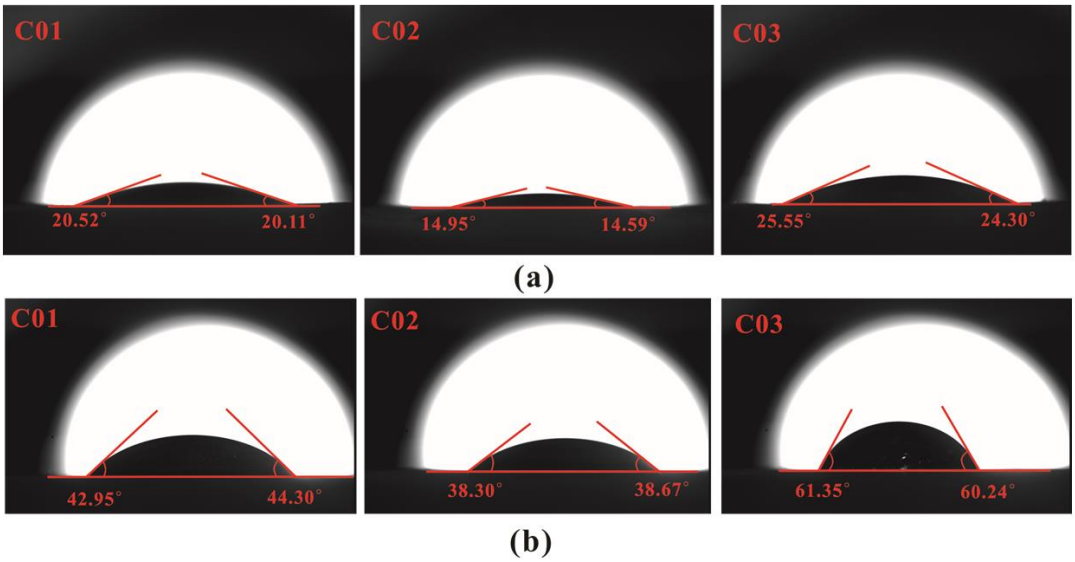

Figure 9. Measured contact angles on the shale surface at room temperature and atmospheric pressure. (a) Deionized water-air contact angle, (b) 1 mol/L NaCl solution-air contact angle. Please refer to Yang and Yu (2020) for a detailed description of the test methods.

The ionic concentration influences not only the surface charge density and zeta potential on the solid surface but also the EDL thickness in the flow channel and therefore changes the electro-kinetic transport properties (Wang et al., 2010). EDL theory predicts that the thickness of the diffuse layer decreases with increasing pore-solution concentration (Studds et al., 1998; Revil & Leroy, 2004; Yang & Yu, 2020). For the 1 mol/L NaCl solution used in this study, the EDL effect on flow can be neglected, as the EDL thickness is very small in comparison with the flow channel diameters. The pressure-dependent electro-viscous effect decreases as the ionic concentration increases and can hardly be present at high salt concentrations (Swartzendruber, 1962). Experiments conducted on microchannels have shown that the flow resistance can reach 20% for a 10^{-4} mol/L KCl solution but can be neglected when a 10^{-2} mol/L KCl solution is used (Li, 2001). Therefore, a decrease in the EDL thickness and electroviscous effect can result in an increase in permeability.

As mentioned above, for the 1 mol/L NaCl solution, the EDL was extremely compressed, and its negative effects on fluid flow could be neglected. If there is no rock deformation or the deformation is negligible under stress, the permeability measured with the NaCl solution would be larger than that measured with deionized water, and the permeability model would be consistent with Eq. (4), behaving as a constant. However, the pore fluid chemistry has a notable influence on

the compressibility behavior of porous media, and an increase in pore solution concentration causes a reduction in compressibility (Ye et al., 2014; Zhang et al., 2016b), which means that the samples saturated with the 1 mol/L NaCl solution were less deformable (lower porosity) than the samples saturated with the deionized water. In addition, the presence of chemicals in the pore fluid reduces the thickness of the EDL and consequently reduces the repulsive forces between minerals. Under the experimental conditions (with a constant confining pressure of 15 MPa and different inlet pressures), the effect of effective pressure on pore structure became prominent due to the changes in the compressibility and reduction in the EDL repulsion forces. The movement of a NaCl solution in shale will not obey Darcy's law with the deformation of the pore structure due to fluid-solid-stress coupling. According to the relationship between the shale porosity and effective stress (Dong et al., 2010), the corresponding permeability model can be expressed as follows:

$$k = \frac{\phi_0 \left(\frac{\sigma_e}{\sigma_0}\right)^{-q} R(\sigma_e)^2}{8\tau} \#(7)$$

where ϕ_0 denotes the porosity under atmospheric pressure (σ_0), σ_e is the effective pressure which is defined as the difference between the confining pressure and pore pressure (Dong et al., 2010; Kwon et al., 2004a), $\mathrm{R}(\sigma_e)$ represents the radius under the effective pressure, and q is a material constant.

Eq. (7) shows that the power function relation between the permeability measured with the 1 mol/L NaCl solution and the pressure gradient is attributed to the change in effective pressure. Among the three samples, sample C03 exhibits the largest compressibility (Table 1), suggesting that this sample was easier to compress and that the pore structure was more sensitive to the change in effective pressure. Thus, the exponent of the permeability vs. pressure gradient curve is largest for sample C03. When the deionized water was used as the permeate, the variation in permeability with the pressure gradient was attributed to the change in the moving ratio or movable water content because EDL repulsion can counterbalance the changes in effective pressure. The exponent β of sample C02 was larger than that of the other two samples, resulting from the fact that sample C02 had a larger bound water content (Yang & Yu, 2020). In addition, when the 1 mol/L NaCl solution was introduced, the compression of the sample under the action of stress led to the further reductions in the porosity and pore throat diameter, thus resulting in a

permeability lower than that of the deionized water. A further decrease in nano-pore size may also result in changes in the properties of a NaCl solution, such as viscosity and structure, and thus increase the TPG.

3.2.4. The effects of mineral composition and pore structure on changes in permeability

Mineral composition and pore structure, which determine the strength of fluid-rock interactions and the size of flow channels, respectively, play a decisive role in controlling the permeability of tight porous media. Minerals differ in their surface properties due to the differences in mineralogy and crystal structure. One of the most important properties of minerals is the strength of their affinity toward water, that is, wettability or hydrophilicity. The wettability of clay minerals, especially montmorillonite and illite, is greater than that of brittle minerals such as quartz and calcite. Shales with a higher strongly hydrophilic mineral content tend to have stronger fluid-rock interactions, resulting in a lower permeability. Experiments performed on fault gouges also indicate that water permeability decreases with an increasing proportion of clay (Takahashi et al., 2007; Crawford et al., 2008). In this work, the minerals in the samples are mainly quartz, clay and carbonate minerals, with trace amounts of feldspar and pyrite. To analyze the effect of mineral composition on the changes in permeability, the relationships between the major mineral constituents and permeability reduction magnitude are shown in Figure 10.

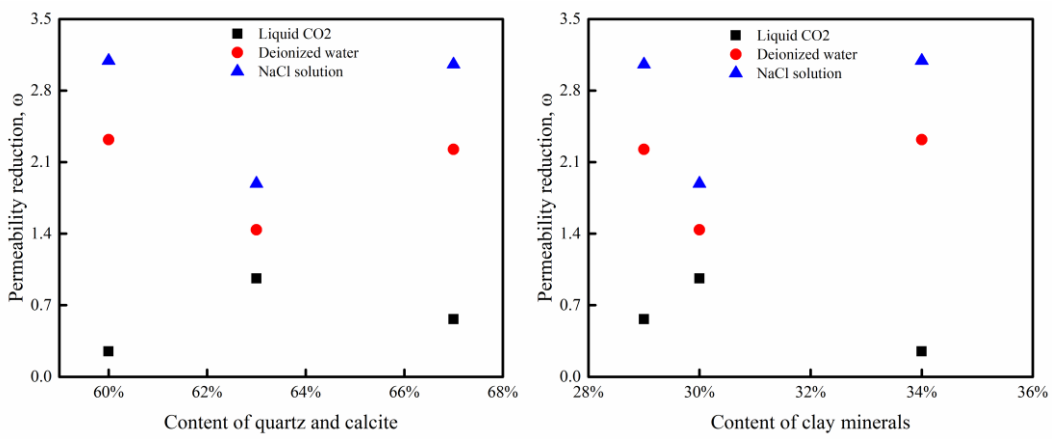

(a) (b)

Figure 10. The relationship between the major mineral constituents and permeability reduction, (a) quartz and calcite, (b) illite and smectite.

As illustrated in Figure 10, both the brittle mineral (quartz and calcite) and clay mineral contents are poorly correlated with the permeability reduction magnitude. The effect of the mineral composition on the liquid CO_2 permeability reduction magnitude is opposite to that of the mineral composition on the deionized water and NaCl solution permeability reduction magnitudes. This may be attributed to the difference in the fluid properties (viscosity and polarity) and in the strength of the fluid-rock interactions. Behnsen and Faulkner (2011) measured the water and argon permeabilities of eight phyllosilicate powers (including kaolinite, illite, smectite, talc and muscovite) at room temperature. The results show that smectite exhibits the largest difference between argon and water permeability (up to 1.8 orders of magnitude), while the differences for illite, kaolinite, muscovite decrease in turn, and talc (the most hydrophobic mineral tested) exhibits the smallest difference (0.4 orders of magnitude). Based on these findings, it is inferred that the samples with a higher content of clay minerals tended to have a larger reduction magnitude between the helium absolute permeability and water permeability. Figure 10(b) shows some implications of this trend, but a quantitative relationship needs to be further studied.

By comparison, the influence of pore structure on the shale permeability is more direct and significant. Porosity, specific surface area, pore radius and pore connectivity play a key role in the magnitude of permeability, as shown by the Kozeny-Carman formula (Revil & Cathles, 1999). In this study, correlations between permeability reduction magnitude and specific surface area and porosity were established. As presented in Figure 11, the permeability reduction magnitudes of the deionized water and NaCl solution are positively related to the specific surface area and porosity, while liquid CO_2 shows the opposite relations. Water adsorption on shale minerals is strengthened by the presence of nanometer-sized pores due to the large specific surface areas (Wang & Yu, 2020). The larger the surface area and porosity of a sample are, the higher the content of bound water, thus increasing the permeability reduction magnitude. Compared with deionized water, the adsorption capacity of liquid CO_2 on shales is relatively small due to the weak polarity and low dielectric constant. The negative effects of adsorption on fluid flow become more prominent when the sample has a lower porosity and a higher proportion of micro-mesopores; in this case, the permeability reduction magnitude would be larger. In addition, a higher specific surface area and porosity are usually related to a larger compressibility (Table 2). The change in pore structure is

considerable under the action of stress when NaCl solution is used as the permeate, which leads to a notable reduction in permeability.

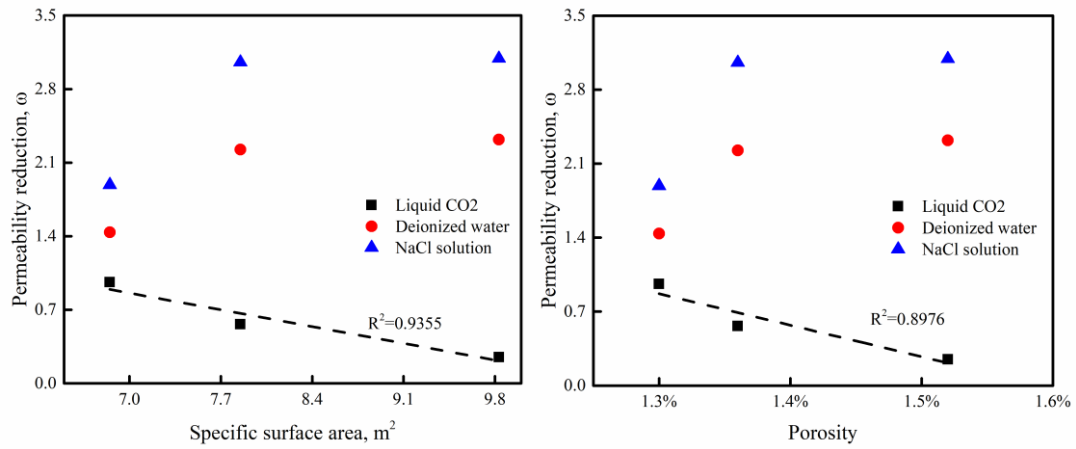

(a) (b)

Figure 11. The dependence of pore structure on permeability reduction magnitude, (a) specific surface area, and (b) porosity.

4. Conclusions

A series of experiments were conducted to investigate the role of fluid types in shale liquid permeability using helium, deionized water, and liquid CO_2 as well as 1 mol/L NaCl solution as permeates. The conclusions of the experiments are as follows.

The three liquids show distinct flow behaviors in shale due to the differences in fluid properties and the strength of the fluid-rock interactions. The liquid CO_2 flow obeys Darcy's law, and no TPG is observed. In contrast, the movement of the deionized water and NaCl solution deviates from Darcy's law, and the TPG is observed. The relationship between the flow rate and pressure gradient can be described by $Q = \gamma_1(G - G_T)^{\beta_1}$, where γ_1 and β_1 are fitting parameters and G_T is the TPG. When the NaCl solution is used as the permeate, the TPG values of samples C01, C02 and C03 are 0.468 MPa/cm, 0.533 MPa/cm and 0.156 MPa/cm, respectively, which are slightly greater than the TPGs measured with deionized water.

The liquid permeability is the largest for the liquid CO_2, followed by the deionized water, and lowest for the 1 mol/L NaCl solution. For samples C01, C02 and C03, the liquid CO_2 permeabilities are constant, with values of 6.90×10^{-19} m^2, 3.80×10^{-20} m^2 and 1.59×10^{-18} m^2, respectively. The permeabilities measured with the NaCl solution and deionized water exhibit

nearly identical ranges (10^{-20}~10^{-21} m^2), and the permeability is lower for the NaCl solution under the same pressure gradient. Both the deionized water and NaCl solution permeability increase with increasing pressure gradient following a power function: $k = \gamma_2(G - G_T)^{\beta_2}$, where γ_2 and β_2 are fitting parameters related to the sample properties.

According to the derivation of the water permeability model that takes into account the simultaneous movement of bulk water and bound water with non-Newtonian behavior, it is argued that the dependence of deionized water permeability on the pressure gradient and the TPG results from the changes in water movability, while the power function relationship between the NaCl solution permeability and pressure gradient is attributed to the changes in pore size caused by variations in effective pressure. Thus, for deionized water tests, the exponent β_2 is the largest for sample C02, which has more mesopores and more hydrophilic minerals than the other samples. When the NaCl solution is introduced as the pore fluid, the exponent β_2 is the largest for sample C03, which has the largest compressibility.

The permeability reduction magnitude (ω) is defined to represent the difference between the liquid permeability and helium absolute permeability. The mineral composition and pore structure play a key role in the magnitude of ω. For the shale samples used in this study, ω ranges from 0.25~0.96 when liquid CO_2 is used as the permeate due to its weak polarity and strong adsorption capacity; ω ranges from 1.44~2.32 when deionized water is used as the permeate because the water molecules are susceptible to interacting with the shale surface to form bound water; ω ranges from 1.89~3.09 when NaCl solution is used as permeate, which is attributed to the pore compression caused by the decreased EDL repulsion force. These results further indicate that the movement of fluids in geological media is a process of fluid-solid-stress coupling.

Acknowledgements

The authors are very grateful for the help from the Rock Fracture WorkGroup. This study was funded by the National Natural Sciences Foundation of China (Grant Nos. 41272387, U1612441 and 41877196) and the Fundamental Research Funds for the Central Universities of China (Grant Nos. 53200759754, 53200759896). The data used in this study is available online: https://doi.org/10.6084/m9.figshare.13585208.v1.

Appendix A: Water permeability model

This work adopts the cylindrical pore assumption to establish a water permeability model that considers the simultaneous movement of free water and bound water with non-Newtonian behavior. Based on the differences in interfacial force and movability, Yang and Yu (2020) divided the water in shale into the strongly bound water (*L1*), inner layer of weakly bound water (*L2*), outer layer of weakly bound water (*L3*) and free water (*L4*) (Figure A1). Correspondingly, the pores are also classified into four types according to the distribution of water with different movability. Among them, pores with radii less than *sp* are filled with strongly bound water and thus do not participate in flow; pores with radii larger than *sp* but smaller than *tp* contribute to flow when the pressure gradient is larger than the TPG; pores with radii larger than *tp* contribute to flow regardless of how small the applied pressure gradient is. The *sp*, *tp* and *fp* represent the distances from the solid surface to the shear plane, threshold plane and free plane, respectively (Yang & Yu, 2020). The model parameters are described in Figure A1.

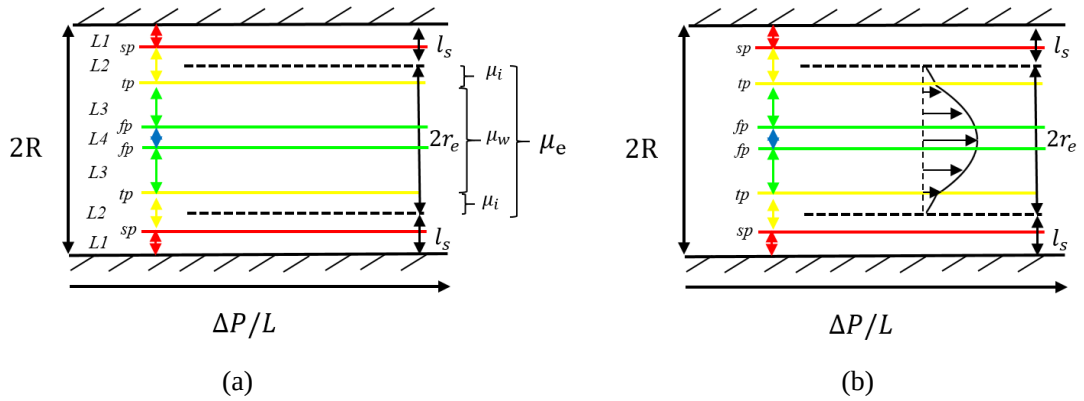

Figure A1. (a) The distribution of water with four different movability as well as the corresponding model parameters in a cylinder pore. The flow zone consists of the Newtonian fluid area (*L3*+*L4*, the viscosity is μ_w) and Bingham fluid area (part of *L2*, the viscosity is μ_i). *R* is the pore radius, l_s is the thickness of immobile layer, r_e is the flow radius ($r_e = R - l_s$), μ_e is the effective viscosity of the flow area, ΔP is the pressure difference and *L* is the length. (b) The velocity distribution of seepage section with an inflection point at the threshold plane.

In the region occupied by Newtonian fluid, the external force equals the viscous force when the movement of water reaches the steady state (Figure A1):

$$\Delta P \cdot \pi r^2 = -\mu_w \cdot 2\pi r L \cdot \frac{dv_1}{dr} \#(A1)$$

where v_1 is the velocity at a distance of r from the pore centerline ($r < r_{tp}$, where r_{tp} is the distance from the pore centerline to the threshold plane). Integrating, v_1 can be described as:

$$v_1 = -\frac{\Delta P}{4\mu_w L} r^2 + C_1 \#(A2)$$

where C_1 is the integration constant. The boundary conditions for the region of Newtonian fluid are $r = r_{tp}$, and $v_1 = v_{tp}$. Thus, the constant C_1 is given by the following expression:

$$C_1 = \frac{\Delta P}{4\mu_w L} r_{tp}^2 + v_{tp} \#(A3)$$

Then, Eq. (A2) can be written as follows:

$$v_1 = \frac{\Delta P\left(r_{tp}^2 - r^2\right)}{4\mu_w L} + v_{tp} \#(A4)$$

For the region occupied by bound water with non-Newtonian behavior, the rheological equation is expressed as:

$$f = f_0 + \mu_i \left(-\frac{dv_2}{dr}\right) \#(\text{A5a})$$

$$-\frac{dv_2}{dr} = \frac{f - f_0}{\mu_i} \#(A5b)$$

where f is the shear stress, f_0 is the critical yield strength (f_0 becomes 0 under Newtonian flow), and v_2 is the velocity at a distance of r from the pore centerline ($r > r_{tp}$). The external force equals to the viscous force when the flow reaches the steady state:

$$\Delta \mathrm{P} \cdot \pi r^2 = 2\pi \mathrm{r} \mathrm{L} \cdot f \#(\text{A6a})$$

$$f = \frac{\Delta P \cdot r}{2L} \#(A6b)$$

Combining Eq. (A5b) and Eq. (A6b) yields the following equation:

$$-\mathrm{d}v_2 = \left[\frac{\Delta P \cdot \mathrm{r}}{2L\mu_i} - \frac{f_0}{\mu_i}\right] dr \#(A7)$$

Integrating, v_2 can be described as:

$$-v_2 = \frac{\Delta P r^2}{4L\mu_i} - \frac{f_0}{\mu_i} r + C_2 \#(A8)$$

where C_2 is the integration constant. The boundary conditions for the region of non-Newtonian fluid are $r = r_e$ and $v_2 = 0$. Thus, the C_2 can be written as:

$$\mathrm{C}_2 = \frac{f_0}{\mu_i} r_e - \frac{\Delta P r_e^2}{4L\mu_i} \#(A9)$$

Combining Eq. (A8) and Eq. (A9), the v_2 can be expressed as:

$$v_2 = \frac{\Delta P(r_e^2 - r^2)}{4\mu_i L} - \frac{f_0}{\mu_i}(r_e - r) \#(A10)$$

According to the boundary condition: $r = r_{tp}$, $v_2 = v_1 = v_{tp}$, the expression of v_{tp} becomes:

$$v_{tp} = \frac{\Delta P\left(r_e^2 - r_{tp}^2\right)}{4\mu_i L} - \frac{f_0}{\mu_i}\left(r_e - r_{tp}\right) \#(\mathrm{A11})$$

Using Eq. (A4), Eq. (A10) and Eq. (A11), the equation of the cross-sectional velocity distribution is obtained as a piecewise function. The corresponding velocity distribution diagram is presented in Figure A1(b).

$$v = \begin{cases} v_1 = \dfrac{\Delta P\left(r_{tp}^2 - r^2\right)}{4\mu_w L} + \dfrac{\Delta P\left(r_e^2 - r_{tp}^2\right)}{4\mu_i L} - \dfrac{f_0}{\mu_i}\left(r_e - r_{tp}\right) & 0 < r \le r_{tp} \\ v_2 = \dfrac{\Delta P(r_e^2 - r^2)}{4\mu_i L} - \dfrac{f_0}{\mu_i}(r_e - r) & r_{tp} \le r \le r_e \end{cases} \#(\mathrm{A12})$$

According to Eq. (A12), the flow rate (Q) through the cylindrical pore can be defined as:

$$\mathrm{Q} = \int_0^{r_e} v dA = \int_0^{r_{tp}} 2\pi r v_1 dr + \int_{r_{tp}}^{r_e} 2\pi r v_2 dr \#(\mathrm{A13a})$$

$$Q_1 = \int_0^{r_{tp}} 2\pi r v_1 dr \#(\mathrm{A13b})$$

$$Q_2 = \int_{r_{tp}}^{r_e} 2\pi r v_2 dr \#(A13c)$$

where Q_1 and Q_2 are the flow rates through the Newtonian fluid area and Bingham fluid area, respectively.

Combining Eq. (A12) and Eq. (A13), Q_1 and Q_2 can be calculated with the following expressions:

$$Q_1 = \frac{\pi r_{tp}^4 \Delta P}{8\mu_w L} + \pi r_{tp}^2 \left[\frac{\Delta P\left(r_e^2 - r_{tp}^2\right)}{4\mu_i L} - \frac{f_0}{\mu_i}\left(r_e - r_{tp}\right)\right] \#(\mathrm{A14a})$$

$$Q_2 = \pi\left(\frac{\Delta P r_e^2}{4\mu_i L} - \frac{f_0 r_e}{\mu_i}\right)\left(r_e^2 - r_{tp}^2\right) + 2\pi\frac{f_0}{\mu_i}\left(\frac{r_e^3 - r_{tp}^3}{3}\right) - \frac{\pi\Delta P}{8\mu_i L}\left(r_e^4 - r_{tp}^4\right) \#(A14b)$$

Combining Eq. (A14a) and Eq. (A4b), Eq. (A13a) then becomes:

$$\mathrm{Q} = \frac{\pi r_{tp}^4 \Delta P}{8\mu_w L} + \frac{\pi\Delta P\left(r_e^4 - r_{tp}^4\right)}{8\mu_i L} + \frac{\pi f_0\left(r_{tp}^3 - r_e^3\right)}{3\mu_i} \#(\mathrm{A15})$$

Assuming that the cross-sectional area of a rock is A, and there is a set of n capillaries with the same radius R per unit area, the flow rate (Q_r) through a rock can be described as:

$$Q_r = nA\left[\frac{\pi r_{tp}^4 \Delta P}{8\mu_w L} + \frac{\pi\Delta P\left(r_e^4 - r_{tp}^4\right)}{8\mu_i L} + \frac{\pi f_0\left(r_{tp}^3 - r_e^3\right)}{3\mu_i}\right] \#(\mathrm{A16})$$

The flow rate (Q_D) using Darcy's law is:

$$\mathrm{Q}_D = \frac{kA\Delta P}{\mu_e L} \#(\mathrm{A17})$$

where k is the permeability.

Combining Eq. (A16) and Eq. (A17), the permeability k then becomes:

$$k = n\pi\left[\frac{\mu_e r_{tp}^4}{8\mu_w} + \frac{\mu_e\left(r_e^4 - r_{tp}^4\right)}{8\mu_i} + \frac{\mu_e f_0 L\left(r_{tp}^3 - r_e^3\right)}{3\mu_i \Delta P}\right] \#(\text{A18})$$

The porosity (ϕ) is defined as follows:

$$\phi = \frac{nA\pi R^2 L_e}{AL} = n\pi\tau R^2 \#(\text{A19})$$

where L_e is the actual seepage length and τ is the tortuosity. Then, Eq. (A18) becomes:

$$k = \frac{\phi}{8\tau R^2}\left[\frac{\mu_e}{\mu_w} r_{tp}^4 + \frac{\mu_e}{\mu_i}\left(r_e^4 - r_{tp}^4\right) + \frac{4}{3}\frac{\mu_e}{\mu_i}\frac{2Lf_0\left(r_{tp}^3 - r_e^3\right)}{\Delta P}\right] \#(A20)$$

A new parameter, effective porosity (ϕ_e), is defined as:

$$\phi_e = \phi\left(1 - \frac{l_s}{R}\right)^2 \#(\text{A21})$$

Combining Eq. (A20) and Eq. (A21), the permeability can be described as:

$$k = \frac{\phi_e}{8\tau}\left[\frac{\mu_e}{\mu_w}\frac{r_{tp}^4}{r_e^2} + \frac{\mu_e}{\mu_i}\left(r_e^2 - \frac{r_{tp}^4}{r_e^2}\right) + \frac{4}{3}\frac{\mu_e}{\mu_i}\frac{2Lf_0\left(r_{tp}^3 - r_e^3\right)}{\Delta P r_e^2}\right] \#(\text{A22})$$

References

Afsharpoor, A., & Javadpour, F. (2016). Liquid slip flow in a network of shale noncircular nanopores. *Fuel*, *180*, 580-590. https://doi.org/10.1016/j.fuel.2016.04.078

Al-Zaidi, E., & Fan, X. (2018). Liquid CO_2 behaviour during water displacement in a sandstone core sample. *Journal of Natural Gas Science and Engineering*, *62*, 259-274. https://doi.org/10.1016/j.jngse.2018.12.005

Armitage, P. J., Faulkner, D. R., Worden, R. H., Aplin, A. C., Butcher, A. R., & Iliffe, J. (2011). Experimental measurement of, and controls on, permeability and permeability anisotropy of caprocks from the CO_2 storage project at the Krechba Field, Algeria. *Journal of Geophysical Research*, *116*, B12208. https://doi.org/10.1029/2011JB008385

Behnsen, J., & Faulkner, D.R. (2011). Water and argon permeability of phyllosilicate powders under medium to high pressure. *Journal of Geophysical Research*, *116*, B12203. https://doi.org/10.1029/2011JB008600

Best, M. E., & Katsube, T. J. (1995). Shale permeability and its significance in hydrocarbon exploration. *The Leading Edge*, *14*(3), 165-170. https://doi.org/10.1190/1.1437104

Borysenko, A., Clennell, B., Sedev, R., Burgar, I., Ralston, J., & Raven, M., et al. (2009).

Experimental investigations of the wettability of clays and shales. *Journal of Geophysical Research: Solid Earth*, *114*, B07202. https://doi.org/10.1029/2008JB005928

Bourg, I. C., & Ajo-Franklin, J. B. (2017). Clay, water, and salt: controls on the permeability of fine-grained sedimentary rocks. *Accounts of Chemical Research*, *50*, 2067-2074. https://doi.org/10.1021/acs.accounts.7b00261

Bourg, I. C., Beckingham, L. E., & Depaolo, D. J. (2015). The nanoscale basis of CO_2 trapping for geologic storage. *Environmental Science & Technology*, *49*(17), 10265-10284. https://doi.org/10.1021/acs.est.5b03003

Busch, A., & Hildenbrand, A. (2013). Predicting capillarity of mudrocks. *Marine and Petroleum Geology*, *45*, 208-223. https://doi.org/10.1016/j.marpetgeo.2013.05.005

Carlos A. León y León. (1998). New perspectives in mercury porosimetry. *Advances in Colloid and Interface Science*, *76-77*, 341-372. https://doi.org/10.1016/S0001-8686(98)00052-9

Chapuis, R.P. (2012). Predicting the saturated hydraulic conductivity of soils: A review. *Bulletin of Engineering Geology & the Environment*, *71*(3), 401-434. https://doi.org/10.1007/s10064-012-0418-7

Crawford, B. R., Faulkner, D. R., & Rutter, E. H. (2008). Strength, porosity, and permeability development during hydrostatic and shear loading of synthetic quartz-clay fault gouge. *Journal of Geophysical Research*, *113*, B03207. https://doi:10.1029/2006JB004634

Dewhurst, D. N., Aplin, A. C., & Sarda, J. P. (1999). Influence of clay fraction on pore-scale properties and hydraulic conductivity of experimentally compacted mudstones. *Journal of Geophysical Research*, *104*(B12), 29261-29274. https://doi.org/10.1029/1999JB900276

Dong, J., Hsu, J., Wu, W., Shimamoto, T., Hung, J., & Yeh, E., et al. (2010). Stress-dependence of the permeability and porosity of sandstone and shale from TCDP hole-A. *International Journal of Rock Mechanics & Mining Sciences*, *47*(7), 1141-1157. https://doi.org/10.1016/j.ijrmms.2010.06.019

Dong, M., Li, Z., Li, S., & Yao, J. (2012). Permeabilities of tight reservoir cores determined for gaseous and liquid CO_2 and C_2H_6 using minimum backpressure method. *Journal of Natural Gas Science & Engineering*, *5*, 1-5. https://doi.org/10.1016/j.jngse.2011.08.006

Fakher, S., & Imqam, A. (2020).High pressure-high temperature carbon dioxide adsorption to

shale rocks using a volumetric method. *International Journal of Greenhouse Gas Control*, *95*, 102998. https://doi.org/10.1016/j.ijggc.2020.102998

Ghanizadeh, A., Gasparik, M., Amann-Hildenbrand, A., Gensterblum, Y., & Krooss, B. M. (2014). Experimental study of fluid transport processes in the matrix system of the European organic-rich shales: I. Scandinavian Alum Shale. *Marine and Petroleum Geology*, *51*, 79-99. https://doi.org/10.1016/j.marpetgeo.2013.10.013

Hildenbrand, A., Schlomer, S., Krooss, B. M., & Littke, R. (2004). Gas breakthrough experiments on pelitic rocks: comparative study with N_2, CO_2 and CH_4. *Geofluids*, *4*, 61-80. https://doi.org/10.1111/j.1468-8123.2004.00073.x

Holt, R. M., & Kolsto, M. I. (2017). How does water near clay mineral surfaces influence the rock physics of shales? *Geophysical Prospecting*, *65*, 1615-1629. https://doi.org/10.1111/1365-2478.12503

Iglauer, S. (2017). CO_2-water-rock wettability: variability, influencing factors, and implications for CO_2 geostorage. *Accounts of Chemical Research*, *50*(5), 1134-1142. https://doi.org/10.1021/acs.accounts.6b00602

Kwon, O., Kronenberg, A. K., Gangi, A. F., Johnson, B., & Herbert, B.E. (2004a). Permeability of illite-bearing shale: 1. Anisotropy and effects of clay content and loading. *Journal of Geophysical Research*, *109*, B10205. https://doi.org/10.1029/2004JB003052

Kwon, O., Herbert, B. E., & Kronenberg, A. K. (2004b). Permeability of illite-bearing shale: 2. Influence of fluid chemistry on flow and functionally connected pores. *Journal of Geophysical Research*, *109*, B10206. https://doi.org/10.1029/2004JB003055

Latief, F. D. E., & Fauzi, U. (2012). Kozeny–Carman and empirical formula for the permeability of computer rock models. *International Journal of Rock Mechanics & Mining Sciences*, *50*, 117-123. https://doi.org/10.1016/j.ijrmms.2011.12.005

Levy, A., Andelman, D., & Orland, H. (2012). The dielectric constant of ionic solutions: A field-theory approach. *Physical Review Letters*, *108*(22), 227801. http://dx.doi.org/10.1103/PhysRevLett.108.227801

Li, D. (2001). Electro-viscous effects on pressure-driven liquid flow in microchannels. *Colloids and Surfaces A: Physicochemical and Engineering Aspects*, *195*(1-3), 35-57.

https://doi.org/10.1016/S0927-7757(01)00828-7

Loucks, R. G., Reed, R. M., Ruppel, S. C., & Hammes, U. (2012). Spectrum of pore types and networks in mudrocks and a descriptive classification for matrix-related mudrock pores. *AAPG Bulletin*, *96*(6), 1071-1098. https://doi.org/10.1306/08171111061

Lundin, M. D., Danby, A. M., Akien, G. R., Binder, T. P., & Subramaniam, B. (2015). Liquid CO_2 as a safe and benign solvent for the ozonolysis of fatty acid methyl esters. *ACS Sustainable Chemistry & Engineering*, *3*(12), 3307-3314. https://doi.org/10.1021/acssuschemeng.5b00913

Mesri, G., & Olson, R. (1971). Mechanisms controlling the permeability of clays. *Clays Clay Minerals*, *19*, 151–158. https://doi.org/10.1346/CCMN.1971.0190303.

Middleton, R. S., Carey, J. W., Currier, R. P., Hyman, J. D., Kang, Q., & Karra, S., et al. (2015). Shale gas and non-aqueous fracturing fluids: Opportunities and challenges for supercritical CO_2. *Applied Energy*, *147*, 500-509. http://dx.doi.org/10.1016/j.apenergy.2015.03.023

Neuzil, C. E. (2013). Can shale safely host U.S. nuclear waste? *Eos Transactions American Geophysical Union*, *94*(30), 261-268. https://doi.org/10.1002/2013EO300001

Pan, B., Jones, F., Huang, Z., Yang, Y., Li, Y., & Hejazi, S. H., et al. (2019). Methane (CH_4) wettability of clay-coated quartz at reservoir conditions. *Energy & Fuels*, *33*, 788-795. https://doi.org/10.1021/acs.energyfuels.8b03536

Ren, X., Zhao, Y., Deng, Q., Li, D., & Wang, D. (2016). A relation of hydraulic conductivity-void ratio for soils based on Kozeny-Carman equation. *Engineering Geology*, *213*, 89-97. https://doi.org/10.1016/j.enggeo.2016.08.017

Revil, A., & Leroy, P. (2004). Constitutive equations for ionic transport in porous shales. *Journal of Geophysical Research*, *109*, B03208. https://doi.org/10.1029/2003JB002755

Revil, A., & Cathles, L. M. (1999). Permeability of shaly sands. *Water Resources Research*, *35*(3), 651-662. https://doi.org/10.1029/98WR02700

Revil, A., Woodruff, W. F., & Lu, N. (2011), Constitutive equations for coupled flows in clay materials. *Water Resources Research*, *47*, W05548. https://doi.org/10.1029/2010WR010002

Roshan H., Ehsani S., Marjo C.E., Andersen M.S., & Acworth R.I. (2015). Mechanisms of water adsorption into partially saturated fractured shales: An experimental study. *Fuel*, *159*,

628-637. https://doi.org/10.1016/j.fuel.2015.07.015

Roshan, H., Al-Yaseri, A. Z., Sarmadivaleh, M., & Iglauer, S. (2016). On wettability of shale rocks. *Journal of Colloid and Interface*, *475*, 104-111. http://dx.doi.org/10.1016/j.jcis.2016.04.041

Sander, R., Pan, Z., & Connell, L. D. (2017). Laboratory measurement of low permeability unconventional gas reservoir rocks: A review of experimental methods. *Journal of Natural Gas Science and Engineering*, *37*, 248-279. http://dx.doi.org/10.1016/j.jngse.2016.11.041

Song, J., & Zhang, D. (2013). Comprehensive review of caprock-sealing mechanisms for geologic carbon sequestration. *Environmental Science & Technology*, *47*, 9-22. https://doi.org/10.1021/es301610p

Song, W., Yao, J., Li, Y., Sun, H., Zhang, L., & Yang, Y., et al. (2016). Apparent gas permeability in an organic-rich shale reservoir. *Fuel*, *181*, 973-984. https://doi.org/10.1016/j.fuel.2016.05.011

Studds, P. G., Stewart, D. I., & Cousens, T. W. (1998). The effects of salt solutions on the properties of bentonite-sand mixtures. *Clay Minerals*, *33*(4), 651-660. https://doi.org/10.1180/000985598545804

Swartzendruber, D. (1962). Non-Darcy flow behavior in liquid-saturated porous media. *Journal of Geophysical Research*, *67*(13), 5205-5213. https://doi.org/10.1029/JZ067i013p05205

Takahashi, M., Mizoguchi, K., Kitamura, K., & Masuda, K. (2007). Effects of clay content on the frictional strength and fluid transport property of faults. *Journal of Geophysical Research*, *112*, B08206. https://doi.org/10.1029/2006JB004678

Tanikawa, W., & Shimamoto, T. (2009). Comparison of Klinkenberg-corrected gas permeability and water permeability in sedimentary rocks. International *Journal of Rock Mechanics and Mining Sciences*, *46*(2), 229-238. https://doi.org/10.1016/j.ijrmms.2008.03.004

Tokunaga, T. K. (2009). Hydraulic properties of adsorbed water films in unsaturated porous media. *Water Resources Research*, *45*, W06415. https://doi.org/10.1029/2009WR007734.

Tokunaga, T. K. (2011). Physicochemical controls on adsorbed water film thickness in unsaturated geological media. *Water Resources Research*, *47*, W08514. https://doi.org/10.1029/2011WR010676

Tokunaga, T. K., & Wan, J. (2013). Capillary pressure and mineral wettability influences on

reservoir CO_2 capacity. *Reviews in Mineralogy and Geochemistry*, *77*(1), 481-503. https://doi.org/10.2138/rmg.2013.77.14

Van Noort, R., & Yarushina, V. (2018). Water, CO_2 and argon permeabilities of intact and fractured shale cores under stress. *Rock Mechanics and Rock Engineering*, *52*, 299-319. https://doi.org/10.1007/s00603-018-1609-8

Wang, J., Liu, H., Wang, L., Zhang, H., Luo, H., & Gao, Y. (2015). Apparent permeability for gas transport in nanopores of organic shale reservoirs including multiple effects. *International Journal of Coal Geology*, *152*(3), 50-62. https://doi.org/10.1016/j.coal.2015.10.004

Wang, L., & Yu, Q. (2016). The effect of moisture on the methane adsorption capacity of shales: A study case in the eastern Qaidam Basin in China. *Journal of Hydrology*, *542*, 487-505. https://doi.org/10.1016/j.jhydrol.2016.09.018

Wang, M., & Yu, Q. (2020). Comparing the permeability of dry and moisturized crushed shales determined by the dynamic process data of methane adsorption. *Journal of Hydrology*, *590*, 125375. https://doi.org/10.1016/j.jhydrol.2020.125375

Wang, M., Chang, C. C., & Yang, R. J. (2010). Electroviscous effects in nanofluidic channels. *The Journal of Chemical Physics*, *132*, 024701. https://doi.org/10.1063/1.3290814

Wei, G., Wen, H., Deng, J., Ma, L., & Liu, Y. (2021). Liquid CO_2 injection to enhance coalbed methane recovery: An experiment and in-situ application test. *Fuel*, *284*, 119043. https://doi.org/10.1016/j.fuel.2020.119043

Wei, K. K., Morrow, N. R., & Brower, K. R. (1986). Effect of fluid, confining pressure, and temperature on absolute permeabilities of low-permeability sandstones. *SPE Formation Evaluation*, *1*(04), 413-423. https://doi.org/10.2118/13093-PA

Wilson, M. J., & Wilson, L. (2014). Clay mineralogy and shale instability: an alternative conceptual analysis. *Clay Minerals*, *49*(2), 127-145. https://doi.org/10.1180/claymin.2014.049.2.01

Yang, S., & Yu, Q. (2020). Experimental investigation on the movability of water in shale nanopores: A case study of Carboniferous shale from the Qaidam Basin, China. *Water Resources Research*, *56*, e2019WR026973. https://doi.org/10.1029/2019WR026973

Yang, Y., & Aplin, A. C. (2007). Permeability and petrophysical properties of 30 natural

mudstones. *Journal of Geophysical Research*, *112*, B03206. https://doi.org/10.1029/2005jb004243

Yang, Y., & Aplin, A.C. (2010). A permeability-porosity relationship for mudstones. *Marine and Petroleum Geology*, *27* (8), 1692-1697. https://doi.org/10.1016/j.marpetgeo.2009.07.001

Ye, W. M., Zhang, F., Chen, B., Chen, Y. G., Wang, Q., & Cui, Y. J. (2014). Effects of salt solutions on the hydro-mechanical behavior of compacted GMZ01 bentonite. *Environmental Earth Sciences*, *72*(7), 2621-2630. https://doi.org/10.1007/s12665-014-3169-x

Zhang, C. P., & Ranjith, P. G. (2018). Experimental study of matrix permeability of gas shale: An application to CO_2-based shale fracturing. *Energies*, *11*, 702. https://doi.org/10.3390/en11040702

Zhang, C. P., Ranjith, P. G., Perera, M. S. A., Zhao, J., Zhang, D., & Wanniarachchi, W. A. M. . (2016a). A novel approach to precise evaluation of carbon dioxide flow behavior in siltstone under tri-axial drained conditions. *Journal of Natural Gas Science and Engineering*, *34*, 331-340. https://doi.org/10.1016/j.jngse.2016.06.074

Zhang, C., & Yu, Q. (2019). Breakthrough pressure and permeability in partially water-saturated shales using methane–carbon dioxide gas mixtures: An experimental study of Carboniferous shales from the eastern Qaidam Basin, China. *AAPG Bulletin*, *103*(2), 273–301. https://doi.org/10.1306/07111818018

Zhang, F., Ye, W. M., Chen, Y. G., Chen, B., & Cui, Y. J. (2016b). Influences of salt solution concentration and vertical stress during saturation on the volume change behavior of compacted GMZ01 bentonite. *Engineering Geology*, *207*, 48-55. https://doi.org/10.1016/j.enggeo.2016.04.010

Zhang, S., & Sheng, J. J. (2017). Effects of salinity and confining pressure on hydration-induced fracture propagation and permeability of Mancos shale. *Rock Mechanics & Rock Engineering*, *50*, 2955-2972. https://doi.org/10.1007/s00603-017-1278-z

Zhang, T., Li, X., Shi, J., Sun, Z., Yin, Y., & Wu, K., et al. (2018). An apparent liquid permeability model of dual-wettability nanoporous media: A case study of shale. *Chemical Engineering Science*, *187*, 280-291. https://doi.org/10.1016/j.ces.2018.05.016